Earth Syst. Dynam., 17, 1779–1798, 2026
https://doi.org/10.5194/esd-17-1779-2026
© Author(s) 2026. This work is distributed under
the Creative Commons Attribution 4.0 License.

Earth System Dynamics
Open Access
EGU

Research article

Drivers of reduced permafrost cooling efficacy of equatorial stratospheric aerosol injection in the Eastern Arctic compared to a moderate emission pathway

Isaline Businger[1], Rhonda C. Müller[1], Raleigh Grysko[1], Jacqueline Oehri[1], Jin-Soo Kim[2], and Gabriela Schaepman-Strub[1]

[1]Department of Evolutionary Biology and Environmental Studies, University of Zurich, Zurich, Switzerland
[2]Department of Civil and Environmental Engineering, Korea Advanced Institute of Science and Technology, Daejeon, Republic of Korea

Correspondence: Isaline Businger (isalinebusinger@bluewin.ch) and Gabriela Schaepman-Strub (gabriela.schaepman@uzh.ch)

Received: 14 March 2026 – Discussion started: 30 March 2026
Revised: 13 August 2026 – Accepted: 16 August 2026 – Published: 24 November 2026

Abstract. The Arctic is warming about four times faster than the global average, with permafrost thaw representing a potential global climate tipping element. Given the insufficient rate of carbon emission reductions, stratospheric aerosol injection (SAI) has emerged as a strategy to abate climate warming. However, its effects on permafrost thaw drivers remain uncertain. The G6sulfur and G6solar experiments, part of the Geoengineering Model Intercomparison Project (GeoMIP6), aim to offset the warming in the high-emission scenario (ssp585) to achieve global-mean near-surface air temperatures comparable to those in the moderate-emission scenario (ssp245), through the injection of stratospheric aerosols near the equator (G6sulfur) or a reduction in top-of-atmosphere solar irradiance (G6solar), respectively. Analyzing both experiments, we find that G6sulfur alters atmospheric circulation, modifying winds, cloud properties, and the North Atlantic Oscillation, which affect temperature patterns and longwave radiation. These changes shift the relative importance of mechanisms driving summer permafrost thaw, resulting in a robust east–west dipole in thaw depth (+0.769 m, 6/6 models): increased thaw in the Eastern Hemisphere (+0.491 m) and a significant but less model-consistent reduction in thaw in the Western Hemisphere (−0.278 m), compared to the ssp245 scenario targeted by the intervention. While both G6sulfur and G6solar slow permafrost decline by 2080–2099 relative to ssp585 ($+4.61 \times 10^6$ and $+5.37 \times 10^6$ km^2 respectively), neither preserves as much permafrost area as ssp245 (-1.08×10^6 km^2 for G6sulfur and -0.32×10^6 km^2 for G6solar). By altering the drivers of permafrost dynamics, G6sulfur creates spatial variations in thaw patterns, resulting in an overall reduction in permafrost area compared to ssp245. Our findings underscore the need to better understand and optimize SAI deployment to avoid unintended regional impacts.

Key points

- By the period 2080–2099, G6sulfur preserves more high-latitude permafrost area than ssp585 but not as much as ssp245
- Spatial impact of G6sulfur on arctic summer permafrost thaw depth: deeper in Eastern and shallower in Western Hemisphere, relative to ssp245
- G6sulfur alters large-scale atmospheric patterns, shifting key Arctic permafrost thaw drivers in the Eastern Hemisphere, relative to ssp245

Published by Copernicus Publications on behalf of the European Geosciences Union.

1 Introduction

The definition of permafrost refers to ground (i.e., soil and rock) that remains at or below 0 °C for a minimum period of two years (ACGR, 1988). In the Northern Hemisphere, the region where permafrost could be expected represents 19 % to 25 % of the Earth's exposed land surface, an area of 18.7 to 24.3×10^6 km^2 (Gruber, 2012). Its considerable presence in high latitudes not only makes permafrost a key component of the Arctic system, but also establishes it as a crucial carbon storage. Current estimates suggest that the northern circumpolar permafrost region stores between 1460 and 1600 Pg of soil organic carbon (Hugelius et al., 2014; Schuur et al., 2022). This is approximately double the current carbon content in the atmosphere and accounts for about half of the total carbon stored in global soils (Strauss et al., 2017).

The Arctic experiences a rate of temperature increase four times faster than the global average (Rantanen et al., 2022). This rapid warming presents a significant risk of thawing to a substantial portion of the cryosphere, including permafrost (Biskaborn et al., 2019). Results from the Coupled Model Intercomparison Project (CMIP6) show that for every 1 °C increase in global mean surface air temperature, the annual mean frozen volume in the top 2 m of soil is predicted to decrease by approximately 10 % to 40 % (Burke et al., 2020). Permafrost acts as a carbon reservoir because low temperatures and frozen conditions limit microbial decomposition of organic matter that has accumulated in soils over thousands of years. As permafrost thaws, previously frozen organic matter becomes available for microbial decomposition, releasing carbon primarily as CO_2 and methane. Under Representative Concentration Pathway 8.5 (RCP8.5), permafrost in northern latitudes is projected to transition from a carbon sink to a carbon source by the end of the 21st century, further contributing to climate warming (McGuire et al., 2018). The carbon release from degradation of the near-surface permafrost under a business-as-usual scenario would create an additional forcing of 0.14 W m^{-2} by 2100, and 0.35 W m^{-2} by 2200, resulting in an additional warming of 0.1 °C, respectively 0.38 °C (Schneider Von Deimling et al., 2012). Further, permafrost is considered a potential climate tipping element because warming-induced thaw can initiate self-reinforcing feedbacks between permafrost degradation, carbon release, and further warming. If critical thresholds are crossed, these feedbacks could lead to substantial and potentially irreversible changes in the permafrost-climate system. Although whether permafrost constitutes a global climate tipping point remains under discussion (Nitzbon et al., 2024), Armstrong McKay et al. (2022) found that the collapse of boreal permafrost could occur at an estimated global warming threshold of 4 °C relative to pre-industrial levels and cause a global-mean surface temperature feedback of about +0.2 to +0.4 °C.

The critical role of Arctic permafrost and the risks posed by its thaw provide an important motivation for understanding the potential effects of climate intervention. However, the motivation for investigating climate intervention extends beyond permafrost, as continued global warming poses broad risk to climate systems, human societies, and natural ecosystems. Global mean temperature rise is projected to reach or exceed 1.5 °C above pre-industrial levels in the near term (IPCC, 2022), with increasing risks of extreme heat, heavy precipitation, drought, sea-level rise, ecosystem disruption, and other climate-related impacts. While reducing greenhouse gas emissions remains essential for limiting these risks, the persistence of climate change has motivated research into additional approaches that could potentially reduce the rate or magnitude of warming. Therefore, several climate intervention methods – approaches that modify aspects of the Earth's climate system to limit global warming – have been proposed as additional solutions alongside emissions mitigation. Stratospheric aerosol injection (SAI) is a solar radiation management technique that mimics the natural cooling effects of volcanic eruptions by injecting sulphate aerosols into the stratosphere (Crutzen, 2006). This method partially reflects the sun's shortwave radiation back into space, thereby cooling the Earth's surface (Jiang et al., 2019). SAI has gained considerable attention in the scientific literature, establishing it as an advanced climate intervention strategy. It is therefore urgent to assess the effectiveness of SAI and its potential impacts, in order to provide policymakers with the critical scientific knowledge necessary for informed decision-making regarding potential SAI research policies and deployment.

This urgency has led to coordinated Earth system modeling efforts to better understand the potential effects of climate interventions. The Geoengineering Model Intercomparison Project (GeoMIP) was established to harmonize research efforts and address the question, "What are the expected climate effects of geoengineering?" (The Geoengineering Model Intercomparison Project (GeoMIP), 2023). The goal is to provide consistency among climate intervention studies and hence facilitate the comparison of results between models (Visioni et al., 2023). Since its creation in 2010, GeoMIP has developed 18 standardized climate model experiments for understanding processes and impacts of solar geoengineering methods.

Building on these coordinated modeling efforts, recent studies have shown that SAI can reduce high-latitude warming and slow permafrost thaw, leading to lower permafrost carbon release (Chen et al., 2020, 2023; Liu et al., 2023). However, its ability to stabilize frozen ground remains uncertain, as it creates regional differences in surface air and soil temperature, rain, and snowfall, which influence the permafrost's response (Lee et al., 2019, 2023; Zhao et al., 2024). SAI also impacts the seasonal cycle, resulting in warmer winters and cooler summers, which may further alter permafrost stability (Jiang et al., 2019). While SAI may slow permafrost degradation, permafrost thaw continues in some regions, particularly where deep soil layers remain insulated

from surface cooling (Morrison et al., 2024b). Natural variability further complicates the picture, making it difficult to detect when and where SAI-induced changes emerge (Morrison et al., 2024a). These uncertainties highlight the need to investigate how the physical mechanisms governing permafrost thermal dynamics respond to SAI, as these processes ultimately determine long-term permafrost stability.

Permafrost freeze-thaw dynamics are influenced by a range of complex and interconnected processes, which may unfold spatially and temporally apart from the injection of stratospheric aerosols. These processes involve radiative fluxes, turbulent heat fluxes, ground heat exchange, precipitation, surface cover, and wind, which in turn are influenced by factors such as surface albedo, cloud cover, air temperature, humidity, soil temperature, vegetation, snow, and ponds (Van Huissteden, 2020).

Although incoming solar radiation is a primary driver, snow cover and vegetation dynamics significantly influence the thermal regime of permafrost. Snow acts as an insulating layer, reducing heat transfer between the ground and the atmosphere (Stieglitz et al., 2003). Therefore, changes in snow cover duration, depth, and density can alter the energy budget at the land surface, affecting the thermal stability of permafrost. Vegetation type has also been identified as an important predictor for components of the surface energy budget during the Arctic summer (Oehri et al., 2022) and influences soil moisture dynamics through evapotranspiration (Ohta et al., 2008). Vegetation changes, such as shifts in species composition, can influence the exchange of energy and water between the land surface and the atmosphere (Eugster et al., 2000).

Furthermore, snow and vegetation have a direct influence on the surface albedo, and hence energy fluxes and permafrost thermal dynamics. Snow cover exhibits seasonal and year-to-year variations, leading to changes in albedo. Also, as snow ages, its albedo decreases compared to fresh snow (Gallet et al., 2011). In the Arctic, the albedo effect is most prominent during spring when the snowpack persists while the sun angle rises (Sturm, 2005). Vegetation cover significantly affects the albedo as well, with boreal forests having a lower albedo compared to shorter vegetation. Similarly, variations in albedo are observed within tundra environments, where dry tundra vegetation tends to have a higher albedo than wet tundra with moist soil or standing water between the vegetation. These differences in albedo can have notable impacts on the net shortwave radiation and, consequently, the energy budget within these ecosystems (Eugster et al., 2000).

Lee et al. (2019) found that under an SAI scenario, precipitation type patterns in high-latitude regions (55–85° N) shift, with reduced rainfall and increased snowfall. Chen et al. (2023) reported similar findings, indicating a decrease in summer precipitation and an increase in winter precipitation in the northern latitudes under SAI. Regarding permafrost, studies show that while SAI can slow the decline of permafrost area, it does not stabilize it (Chen et al., 2023; Lee et al., 2019). The interplay between vegetation, snow cover, and permafrost dynamics is complex and varies spatially and temporally. In this context, understanding how these mechanisms respond to changes in near-surface air temperature under solar geoengineering scenarios is crucial.

While recent studies have documented large-scale atmospheric circulation changes under SAI – including NAO shifts and residual high-latitude warming – and their broad effects on permafrost area, the specific physical pathways through which these atmospheric changes translate into permafrost thaw depth responses have not been systematically identified. In particular, it remains unknown whether permafrost thaw depth under SAI is primarily driven by the intended reduction in shortwave radiation, or by unintended side effects such as changes in atmospheric circulation and longwave radiation trapping, and how driver importance varies seasonally and between hemispheres. Our study therefore aims to understand to what extent stratospheric aerosol injection, as implemented in the GeoMIP G6sulfur scenario, shifts key drivers influencing permafrost freeze-thaw dynamics. We compare the SAI scenarios (G6sulfur and G6solar) with two climate change scenarios (ssp245 and ssp585). We evaluate changes in permafrost area, thaw depth, and related drivers, use variance partitioning to identify key influences, and finally investigate if spatial patterns are linked to shifts in the North Atlantic Oscillation (NAO).

2 Data and Methods

2.1 Model simulations

We assess the impacts of SAI strategies on permafrost thaw and related drivers using output data from the GeoMIP Phase 6 models, with the most recent release being from 2015 (Kravitz et al., 2015). Our analysis specifically focuses on the G6sulfur and G6solar scenarios, simulated by six coupled Earth System Models (ESMs) (Table 1).

Both scenarios are designed to achieve global mean near-surface air temperatures within 0.2 °C of the ssp245 pathway, which therefore serves as the primary baseline for comparison in our study. Importantly, both G6sulfur and G6solar maintain the same CO_2 and other greenhouse gas concentrations as ssp585. The ssp585 scenario provides a reference for a high-emission, business-as-usual trajectory, representing a future without emission mitigation or climate intervention, while ssp245 represents a moderate-emission pathway, assuming the implementation of climate protection measures (O'Neill et al., 2017).

The G6sulfur scenario adjusts the amount of stratospheric aerosol or aerosol precursors injected in each model such that decadal global mean near-surface air temperature remains within 0.2 °C of the ssp245 pathway (Jones et al., 2022). The aerosol injection is concentrated along the 0° longitudinal band, spanning latitudes from 10° S to 10° N, at altitudes between 18 and 20 km across atmospheric model layers.

However, some models do not directly simulate stratospheric aerosol injection and instead prescribe aerosol optical depth (AOD) distributions. For CNRM-ESM2-1, the AOD distributions are provided by GeoMIP, while MPI-ESM1-2-LR and MPI-ESM1-2-HR use AOD distributions based on Niemeier and Schmidt (2017) and Niemeier et al. (2020), respectively, as described by Jones et al. (2022). The G6solar scenario mimics the G6sulfur scenario, but reduces top-of-atmosphere solar irradiance instead of injecting aerosols. Simulations for both scenarios run from 2020 to 2100, as described in Kravitz et al. (2015).

G6sulfur and G6solar were used in parallel to enable a comparison of the impacts of stratospheric aerosol injection and top-of-atmosphere solar irradiance reduction. As the spatial distribution of forcing is expected to show smaller differences among models using G6solar compared to G6sulfur, it enables the determination of uncertainties associated with the transport of stratospheric sulphate aerosols (Visioni et al., 2023).

2.2 Permafrost and permafrost driver analysis

We investigate the permafrost area, summer permafrost thaw depth, and various permafrost drivers, including atmospheric, energy budget, precipitation, soil, and vegetation variables (Table 2). For each ESM and scenario, all available ensemble members are first averaged to produce a model-specific ensemble mean. Each model-specific mean is then bilinearly regridded to a shared resolution of $0.5° \times 0.5°$ using Climate Data Operators (CDO) version 2.3.0 from the Max Planck Institute for Meteorology (Schulzweida, 2023). The six regridded model-specific means are subsequently averaged to obtain the multi-model mean, ensuring each model contributes equally regardless of the number of ensemble members available. Atmospheric 3D variables are vertically interpolated to standard hectopascal (hPa) levels.

Changes in summer permafrost thaw depth and its predictor variables are analyzed for the G6solar and G6sulfur experiments, relative to ssp245 and ssp585. This analysis is performed for the geographical area characterized by a permafrost probability equal to or exceeding 50 %, based on mean annual air temperature (MAAT) projections for the end of the 21st century (2080–2099). To define this region of interest, we apply an observation-based relationship between MAAT and permafrost probability (F_{MAAT}), as initially established by Gruber (2012) and refined in the methodology outlined by Chadburn et al. (2017). The relationship is represented by equation 1:

$$F_{\mathrm{MAAT}} = \frac{1}{2}\mathrm{erfc}\left(\frac{\mathrm{MAAT}+\mu}{\sqrt{2\sigma^2}}\right), \quad (1)$$

where $\mu = 4.38\,°\mathrm{C}$ is the mean, $\sigma = 2.59\,°\mathrm{C}$ is the standard deviation, and erfc denotes the complementary error function, a standard mathematical function that forms part of the transformation of MAAT values into a permafrost probability ranging from 0 to 1.

We assume that any grid cell with F_{MAAT} of 50 % or higher is recognized by the models as containing permafrost (Burke et al., 2020). To ensure this relationship is applied only where it is physically meaningful, we additionally apply two filters: grid cells are retained only if they have a land fraction greater than or equal to 35 % and a grounded ice sheet fraction less than or equal to 65 %. The land fraction threshold excludes grid cells dominated by ocean or water bodies, where permafrost classification is not meaningful, while the grounded ice sheet fraction threshold excludes ice-sheet-dominated cells (e.g., Greenland), where the MAAT-based permafrost probability relationship does not apply. As with any threshold-based filtering approach, these criteria primarily affect coastal and ice-margin grid cells, which represent transitional zones inherently most sensitive to classification choices, regardless of the specific threshold values used.

The permafrost mask used for thaw depth analysis is derived from 2080–2099 MAAT projections under the ssp245 scenario and is applied consistently across all scenario comparisons (G6solar, G6sulfur, and ssp585 relative to ssp245). This ensures that thaw depth differences are evaluated within a common, policy-relevant spatial domain.

Thaw depth is determined using monthly mean soil temperature profiles. Soil temperature data is interpolated between the model's layers to estimate temperatures at specific depths. The thaw depth is then defined as the depth at which the temperature crosses 0 °C (Burke et al., 2020). It is important to note that soil temperature profile resolution varies among models. CNRM-ESM2-1, IPSL-CM6A-LR, and CESM2-WACCM have better-resolved soil profiles (14–25 layers), whereas UKESM1-0-LL, MPI-ESM1-2-HR, and MPI-ESM1-2-LR have coarser soil profiles (4–5 layers; see Table 1), which could introduce biases into the estimates (Chadburn et al., 2015). In particular, UKESM1-0-LL has a maximum soil depth of 2 m, which may limit its ability to simulate very deep active layers under high-emission scenarios. Our multi-model ensemble approach helps mitigate the impact of this individual model limitation on the overall results.

Differences between scenarios are assessed using a paired t-test, based on annual multi-model-mean differences within each 20-year analysis period (2030–2049 and 2080–2099). Because annual permafrost area and thaw depth time series exhibit serial correlation, lag-1 autocorrelation was estimated from detrended annual anomalies following Zwiers and von Storch (1995), and effective sample sizes were calculated prior to applying the test. Since the same six ESMs contribute simulations to all scenarios, model responses are naturally paired rather than independent. To assess inter-model robustness, we complement the time-series analysis with a model-by-model paired comparison of late-century (2080–2099) means for permafrost area and thaw depth (domain-wide Northern High Latitudes, regional Eastern and Western

Table 1. Overview of the six ESMs used in this study, with the number of available simulations, the method of SAI model implementation, the number of soil layers, and the maximum soil depth (m) represented in each model (adapted from Visioni et al., 2021). For details on the implementation of "AOD scaled", see [a] Tilmes et al. (2015), and [b] Niemeier and Schmidt (2017). All models feature interactive marine biogeochemistry and are coupled with an interactive land model.

Model name	Reference(s)	Number of simulations				Stratospheric aerosol in G6sulfur	Number of soil layers	Maximum soil depth [m]
		G6solar	G6sulfur	ssp245	ssp585			
CESM2-WACCM	Danabasoglu et al. (2020) Gettelman et al. (2019)	1	2	4–5	4–5	SO_2 injection	25	42.0
CNRM-ESM2-1	Séférian et al. (2019)	1	2–3	10	5	AOD scaled[a]	14	10.0
IPSL-CM6A-LR	Boucher et al. (2020) Lurton et al. (2020)	1	1	11	7	SO_2 injection	18	65.6
MPI-ESM1-2-HR	Muller et al. (2018)	3	3	2	2	AOD scaled[b]	5	7.0
MPI-ESM1-2-LR	Muller et al. (2018)	3	3	50	50	AOD scaled[b]	5	7.0
UKESM1-0-LL	Sellar et al. (2019)	3	3	6–17	5	SO_2 injection	4	2.0

Hemisphere means, and east–west dipole magnitude). For each comparison, model uncertainty is quantified using bootstrap confidence intervals derived from resampling the six paired model-specific differences, while model consistency is assessed as the percentage of models agreeing on the sign of the difference. In the Results, we report the time-series mean difference as the primary effect size estimate, complemented by bootstrap confidence intervals and model agreement from the paired model-based analysis.

2.3 Variance partitioning analysis

We select 18 predictors (Table 2) spanning three complementary categories of physical controls on permafrost freeze-thaw dynamics: atmospheric forcing, surface energy balance, and land-surface state, together representing the chain of processes that govern the permafrost thermal regime, following the framework described in Van Huissteden (2020). We conduct a variance partitioning analysis (adapted from Oehri et al., 2022) to assess the ability of these 18 selected factors driving permafrost freezing and thawing, to predict the magnitude of summer permafrost thaw depth (SPTD). This method helps mitigate statistical confounding of predictors by distinguishing the variance in SPTD that can be explained jointly or independently by various drivers. To accomplish this, we use the set of 18 selected predictors related to SPTD to construct all possible models comprising three predictors each. For each model, we determine the variance explained by each predictor by averaging its contribution across all possible predictor orderings, using the LMG (Lindeman, Merenda and Gold) method (Lindeman et al., 1980), as described in Grömping (2006) and implemented in R using the relaimpo package. The LMG method is a variance decomposition technique that quantifies the relative importance of each predictor variable in explaining the variance of SPTD while accounting for correlations between predictors. For a linear regression model with k predictors, each predictor's incremental explained variance is computed across all possible orderings, from being entered first (its marginal R^2, ignoring all others) to last (its contribution beyond all others), and then averaged. For a confounded predictor (one correlated with others), the contribution shrinks the later it enters, since the shared variance has already been claimed; for an uncorrelated predictor, it stays roughly constant across orderings. This averaging of each predictor's marginal contribution over all orderings is the key feature of the LMG method that distinguishes it from simple correlation analysis or stepwise regression: it ensures that the contribution of each predictor is fairly assessed regardless of the order in which predictors enter the model, thereby mitigating the effects of multicollinearity among predictors.

The choice of three predictors per model balances the need to assess confounding and shared explanatory structure among predictors while maintaining interpretable model configurations. With 18 predictor variables, constructing all possible models with three predictors yields 816 unique predictor triplets, each tested across 6 possible predictor orderings, resulting in 4896 models in total. An additional advantage of this approach is that each predictor appears across many different triplets, yielding a distribution of explained-variance (LMG) values (Figs. 3 and 5) rather than single estimate. This allows each predictor's typical contribution to be summarized (e.g. using the median and interquartile range), while also quantifying how much its apparent importance varies depending on which other predictors are included. This variability is informative in itself, as it reflects the sensitivity of each predictor's contribution to model composition and thus its susceptibility to collinearity and confounding effects. In contrast, a single model including all 18 predictors would provide only one importance estimate per predictor

and would not reveal this dependence on co-predictor structure.

We then compute the overall average explained variance (%) for each SPTD predictor across all models. We conduct this analysis in two distinct northern high-latitude regions: the Eastern Hemisphere (longitude 0–180°) with 3765 datapoints and the Western Hemisphere (longitude 180–360°) with 4000 datapoints, and during two different seasons: boreal winter (December, January, February; DJF) and summer (June, July, August; JJA), using means over the period 2080–2099.

For each 3D variable (Figs. S1–S8 in the Supplement) that has a latitude/longitude, time, and pressure levels (i.e. clw: mass fraction of cloud liquid water, cli: mass fraction of cloud ice, ua: eastward wind, and va: northward wind), we test its predictive power at different pressure levels (in hPa) using variance partitioning analyses for each region and season, as described above. The pressure level with the highest predictive power for the variation in SPTD is selected for integration into the variance partitioning analysis, alongside the 2D variables (latitude/longitude and time).

In addition to the variance partitioning analysis, we also conduct a Pearson correlation analysis to further investigate the strength and direction of the relationship between SPTD and the selected drivers. This analysis complements the variance partitioning by providing additional insights into the associations between the predictors and SPTD. Both the variance partitioning analysis and the correlation maps of SPTD drivers are performed in R version 4.1.3.

2.4 Correlation with the North Atlantic Oscillation

To test whether spatial patterns of permafrost area, thaw depth, and related drivers are linked to shifts in atmospheric pressure systems, we calculate an indicator for the North Atlantic Oscillation (NAO). The NAO is assessed through the pressure difference between Iceland and the Azores, as outlined by Jones et al. (2021). We utilize the monthly mean sea-level pressure (MSLP) data from 2080 to 2099 from the nearest model grid cells to Stykkishólmur, Iceland (65°05′ N, 22°44′ W), and Ponta Delgada in the Azores (37°44′ N, 25°41′ W). We derive a NAO index by detrending the time series of MSLP at each location, normalizing the resulting anomalies by their standard deviation, and then calculating the difference of the normalized anomalies between G6sulfur and ssp245. The 3-month rolling mean of the NAO index is correlated with the normalized 3-month rolling mean temperature, as well as the mass fraction of cloud liquid water and ice, along 18 geographical segments spanning from 0 to 180° E and 65 to 75° N. Each of these segments covers an area of 10° longitude and 10° latitude.

3 Results

3.1 Evolution of permafrost area under SAI

At the start of the simulation in 2020, the permafrost area derived from the multi-model ensemble mean of MAAT is 13.72×10^6 km^2 for ssp585, 13.22×10^6 km^2 for ssp245, 13.07×10^6 km^2 for G6solar, and 12.49×10^6 km^2 for G6sulfur (Fig. 1a). These results closely align with recent studies summarized in Obu (2021), where the current estimated permafrost area in the Northern Hemisphere ranges between 12.2 and 17.7×10^6 km^2. Under ssp585, permafrost loss is substantial throughout the 21st century. However, SAI (G6solar and G6sulfur) mitigates this decline, resulting in a larger permafrost area compared to ssp585. For the period 2030–2049 (green shaded in Fig. 1a), this difference is significant (P-value < 0.001 for G6solar and P-value $= 0.003$ for G6sulfur), but neither SAI scenario differs significantly from ssp245 in this period (P-value $= 0.549$ for G6solar and P-value $= 0.125$ for G6sulfur) (Fig. 1b). By the end of the simulation (2080–2099, blue shaded in Fig. 1a), permafrost area under SAI continues to be substantially larger than under ssp585, with $+5.37 \times 10^6$ km^2 (P-value < 0.001, bootstrap 95 % CI: $[4.07, 5.47] \times 10^6$ km^2, 6/6 models) for G6solar and $+4.61 \times 10^6$ km^2 (P-value < 0.001, bootstrap 95 % CI: $[3.38, 5.01] \times 10^6$ km^2, 6/6 models) for G6sulfur (Fig. 1c). Compared to ssp245, however, permafrost area under SAI is smaller, with -0.32×10^6 km^2 (P-value < 0.001, bootstrap 95 % CI: $[-0.80, -0.07] \times 10^6$ km^2, 4/6 models) for G6solar and -1.08×10^6 km^2 (P-value < 0.001, bootstrap 95 % CI: $[-1.83, -0.43] \times 10^6$ km^2, 5/6 models) for G6sulfur. This suggests that while SAI helps preserve permafrost relative to ssp585, it does not fully maintain the levels seen under ssp245, the scenario targeted by the SAI climate intervention experiment G6sulfur.

Regionally, the largest difference in permafrost area occurs in the Eastern Hemisphere, specifically between longitudes 90° E and 130° E, bordered by the Central Siberian Plateau to the east and the Verkhoyansk Range to the west (Fig. 1d). In this region, permafrost retreats more rapidly under G6sulfur compared to G6solar and ssp245. Under ssp585, only small patches of permafrost remain along the northern coast of Greenland, the shores of Baffin Bay, and the Far Eastern region of Russia by 2080–2099.

3.2 Difference in thaw depth under SAI

When analyzing changes in permafrost area under varying conditions, thaw depth – representing the extent of seasonal thawing above the permafrost – can be used to study how permafrost responds to SAI, as it provides an important indicator of permafrost stability by reflecting the depth to which previously frozen soil is exposed to seasonal thawing and associated processes such as organic carbon decomposition (Garnello et al., 2021). As expected, following the

Table 2. Overview of the variables used in the six ESMs specified by long name, abbreviation, units, and dimensions being either 2 dimensional (latitude/longitude) or 3 dimensional (latitude/longitude and height in pressure levels (hPa) or depths (m)).

Variable name	Variable ID	Units	Dimensions	Variable name	Variable ID	Units	Dimensions
Near-Surface Air Temperature	tas	K	2D	Surface Downwelling Shortwave Radiation	rsds	$W\,m^{-2}$	2D
Near-Surface Relative Humidity	hurs	%	2D	Surface Upwelling Shortwave Radiation	rsus	$W\,m^{-2}$	2D
Sea Level Pressure	psl	hPa	2D	Surface Downwelling Longwave Radiation	rlds	$W\,m^{-2}$	2D
Near-Surface Wind Speed	sfcWind	$m\,s^{-1}$	2D	Surface Upwelling Longwave Radiation	rlus	$W\,m^{-2}$	2D
Eastward Wind	ua	$m\,s^{-1}$	3D	Surface Upward Sensible Heat Flux	hfss	$W\,m^{-2}$	2D
Northward Wind	va	$m\,s^{-1}$	3D	Surface Upward Latent Heat Flux	hfls	$W\,m^{-2}$	2D
Total Cloud Cover Percentage	clt	%	2D	Moisture in Upper Portion of Soil Column	mrsos	$kg\,m^{-2}$	2D
Precipitation	pr	$kg\,m^{-2}\,s^{-1}$	2D	Leaf Area Index	lai	1	2D
Mass Fraction of Cloud Liquid Water	clw	$kg\,kg^{-1}$	3D				
Mass Fraction of Cloud Ice	cli	$kg\,kg^{-1}$	3D	Temperature of Soil	tsl	K	3D

results of Fig. 1, the trends in permafrost area are directly reflected in thaw depth, with thaw depth statistically being shallower across all regions when comparing the SAI scenarios to ssp585 (bottom row, Fig. 2a and b). Also as anticipated, our analysis shows that both G6solar and G6sulfur result in a deeper domain-mean summer thaw depth at northern high latitudes compared to ssp245 (G6solar: +0.157 m, P-value = 0.008; G6sulfur: +0.190 m, P-value = 0.005), although this domain-mean signal is not robust across models (bootstrap 95 % CI crosses zero for both scenarios, 4/6 models) (top row, Fig. 2a and b). However, regionally, G6sulfur creates a significantly deeper summer thaw depth in the Eastern Hemisphere (+0.491 m, P-value < 0.001, bootstrap 95 % CI: [0.055, 0.582] m, 5/6 models), whereas it results in a shallower summer thaw depth in the Western Hemisphere (−0.278 m, P-value < 0.001), though this signal is less robust across models (bootstrap 95 % CI: [−0.553, 0.070] m, 3/6 models) compared to ssp245. Most notably, the east–west dipole under G6sulfur is robust across all six models (dipole magnitude: +0.769 m, P-value = 0.002, bootstrap 95 % CI: [0.144, 1.033] m, 6/6 models), indicating a consistent spatial reorganization of thaw depth rather than a uniform domain-wide response. As predicted, this pattern also results in a spatial overlap between changes in permafrost area (Fig. 1d) and variations in summer thaw depth (Fig. 2a). These results confirm the findings of Chen et al. (2023), who, using the CLM5 model, observed similar spatial patterns in the permafrost area mapped from the annual maximum active layer thickness. Based on the observed spatial distributions and the significance of the differences, we direct our further investigations towards understanding the underlying processes driving the patterns of summer permafrost thaw depth in the Eastern and Western Hemispheres under G6sulfur, as well as investigating why they do not fully match the ssp245 scenario.

3.3 Drivers of difference in summer permafrost thaw depth of G6sulfur compared to ssp245 scenario

To gain insights into the drivers contributing to the observed variations in summer permafrost thaw depth (SPTD) across the Eastern and Western Hemispheres under G6sulfur conditions compared to ssp245, we conduct both a variance partitioning and a correlation analysis. The variance partitioning analysis quantifies the predictive ability of each selected driver to explain the difference in SPTD observed between G6sulfur and ssp245, while the correlation analysis provides information on the strength and direction of the relationships between SPTD and selected drivers. It is important to note that, since we are examining the difference between a geoengineering experiment and ssp245, the results from the variance partitioning analysis only indicate the explained variance of the difference between the two scenarios, not the absolute explained variance. Therefore, in this study, a low explained variance does not necessarily imply that a specific variable is not an important predictor for summer permafrost thaw depth; rather, it means the explained variance of this variable does not change under SAI conditions. The same principle applies to the correlation analysis and further analyses conducted in this study.

The predictors, explaining the difference in SPTD between G6sulfur and ssp245 in the Eastern Hemisphere, are shown in Fig. 3a and b. The most important in boreal winter are surface downwelling longwave radiation (33.6 %), near-surface air temperature (31.4 %), and northward wind at 20 hPa (31.3 %). These winter drivers reflect NAO-induced warming and longwave trapping effects, as discussed in Sect. 3.4. Factors, such as near-surface air temperature, mass fraction of cloud liquid water and ice, as well as surface upwelling and downwelling longwave radiation display a strong positive correlation to the difference in SPTD, while zonal and meridional winds have a strong negative relationship (Fig. 3c).

As depicted in Fig. 3b, the key summer predictors explaining the difference in SPTD between G6sulfur and ssp245 in the Eastern Hemisphere are northward wind at 150 hPa (37.2 %), eastward wind at 20 hPa (30.4 %), mass fraction of cloud ice at 350 hPa (30.3 %), and mass fraction of cloud liquid water at 300 hPa (23.3 %). These summer drivers reflect altered atmospheric circulation patterns, as discussed in Sect. 3.4. During summer, sea level pressure exhibits a strong positive correlation to the difference in SPTD, whereas wind

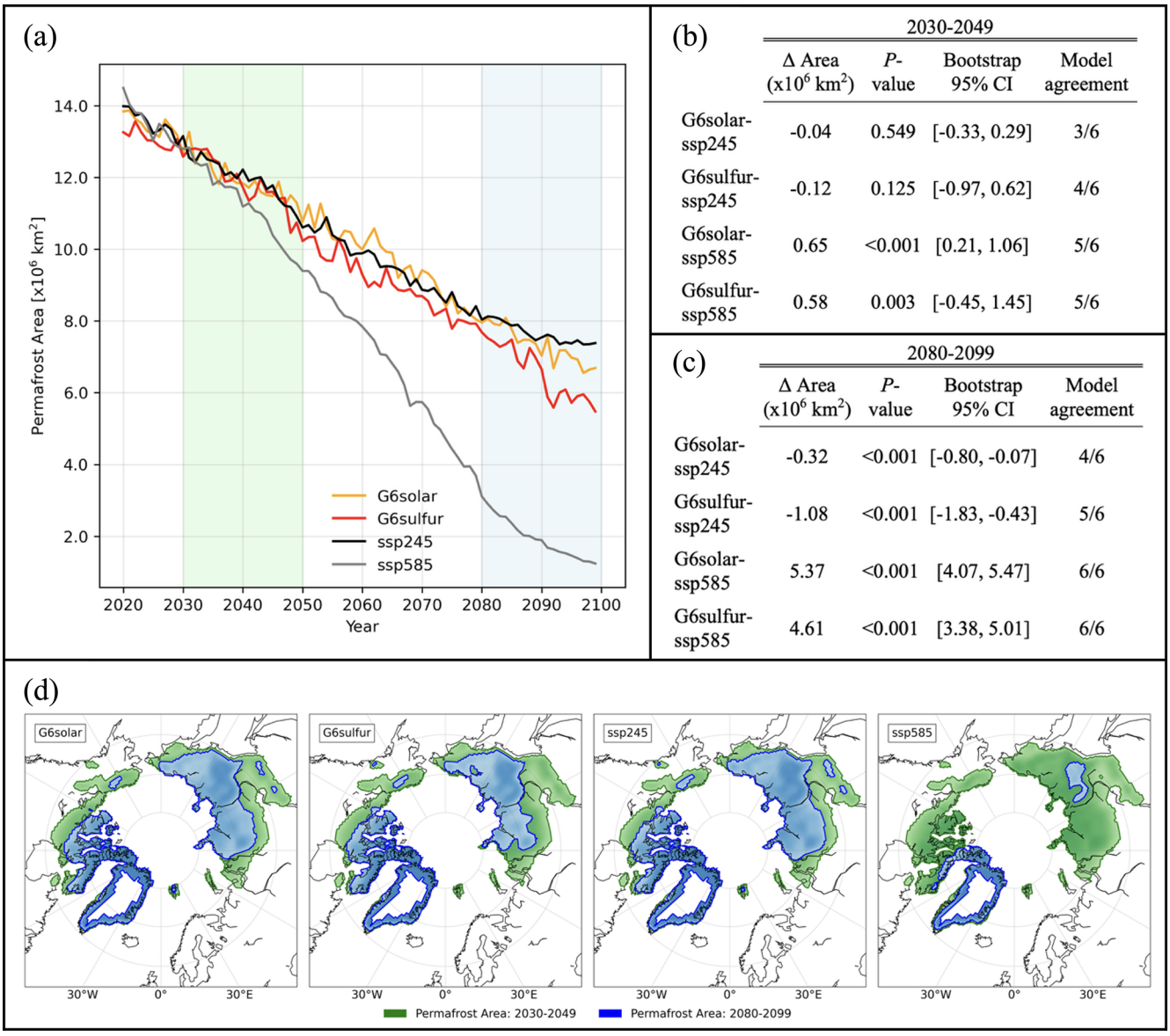

(b) 2030-2049

	Δ Area ($x10^6$ km^2)	*P*-value	Bootstrap 95% CI	Model agreement
G6solar-ssp245	-0.04	0.549	[-0.33, 0.29]	3/6
G6sulfur-ssp245	-0.12	0.125	[-0.97, 0.62]	4/6
G6solar-ssp585	0.65	<0.001	[0.21, 1.06]	5/6
G6sulfur-ssp585	0.58	0.003	[-0.45, 1.45]	5/6

(c) 2080-2099

	Δ Area ($x10^6$ km^2)	*P*-value	Bootstrap 95% CI	Model agreement
G6solar-ssp245	-0.32	<0.001	[-0.80, -0.07]	4/6
G6sulfur-ssp245	-1.08	<0.001	[-1.83, -0.43]	5/6
G6solar-ssp585	5.37	<0.001	[4.07, 5.47]	6/6
G6sulfur-ssp585	4.61	<0.001	[3.38, 5.01]	6/6

Figure 1. Evolution of permafrost area under different scenarios. **(a)** Annual permafrost area from 2020 to 2100 under G6solar, G6sulfur, ssp245, and ssp585 scenarios (including only areas with $F_{MAAT} \geq 50\,\%$). **(b–c)** Difference in mean permafrost area over the periods 2030–2049 and 2080–2099 between G6solar-ssp245, G6sulfur-ssp245, G6solar-ssp585, and G6sulfur-ssp585, together with the *P*-value from the autocorrelation-corrected paired *t*-test of the time-series analysis, the bootstrap 95 % confidence interval, and model agreement (i.e., the proportion of the six ESMs agreeing on the sign of the difference) from the paired model-based analysis (see Sect. 2.2). **(d)** Spatial distribution of permafrost area (including only areas with $F_{MAAT} \geq 50\,\%$) over the period 2030–2049 (green) and 2080–2099 (blue) under G6solar, G6sulfur, ssp245, and ssp585.

speed, zonal and meridional winds, and cloud composition display a strong negative relationship (Fig. 3d).

During the boreal summer, energy fluxes, apart from surface downwelling longwave radiation (10.4 %), are of low importance in explaining the difference in SPTD between G6sulfur and ssp245. This observation is particularly intriguing given that G6sulfur is designed to reduce shortwave radiation through stratospheric aerosol injection. Furthermore, summer vegetation, as indicated by the leaf area index, and moisture in the upper portion of soil column play only a minimal role in explaining the difference in SPTD between G6sulfur and ssp245.

Particularly notable is the complex interplay between cloud water-ice content and thaw depth. We see a positive correlation to SPTD in the winter season and the opposite during the summer season. Furthermore, the predictors mass fraction of cloud liquid water (Fig. S5c and d in the Supplement) and mass fraction of cloud ice (Fig. S7c and d in

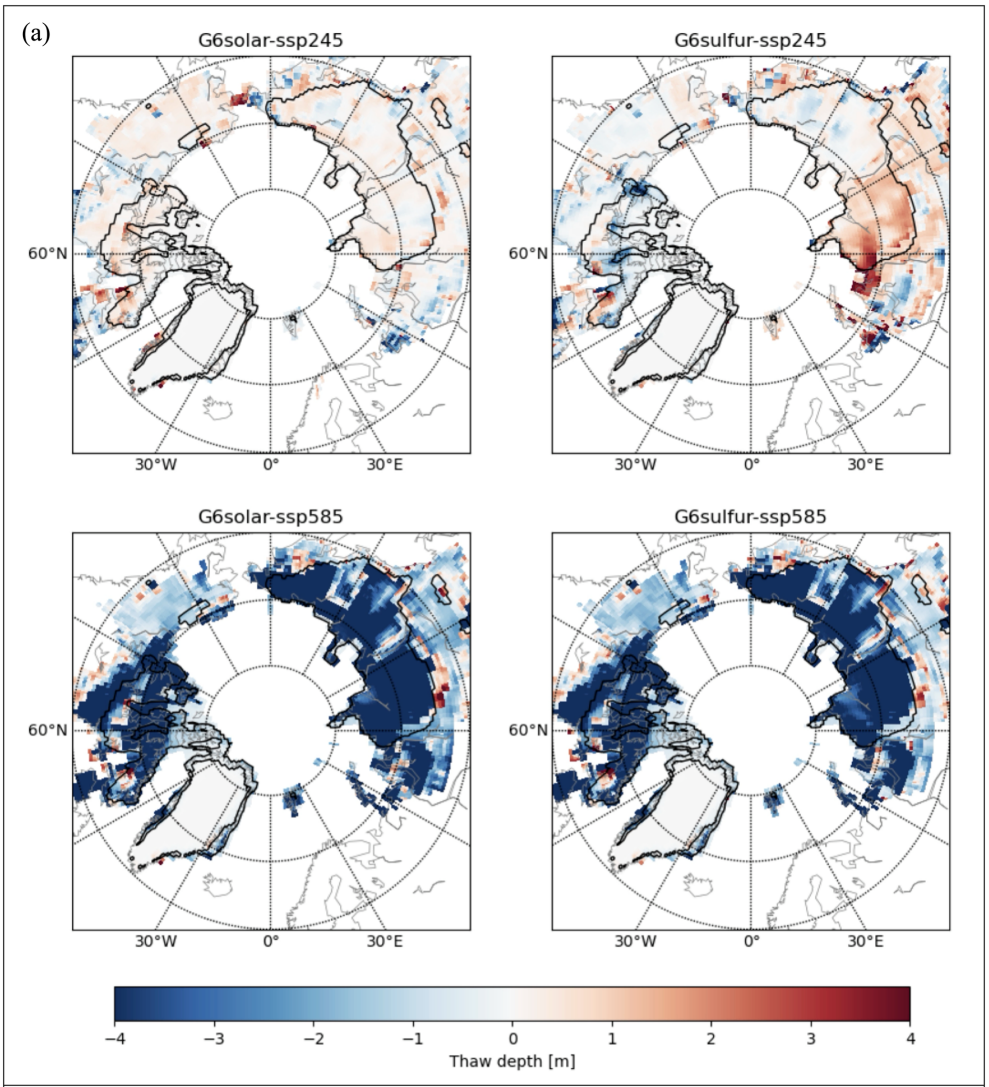

(b)

	G6solar-ssp245				G6sulfur-ssp245			
	Δ Thaw Depth	*P*-value	Bootstrap 95% CI	M.A.	Δ Thaw Depth	*P*-value	Bootstrap 95% CI	M.A.
Northern High Latitudes	0.16	0.008	[-0.04, 0.49]	4/6	0.19	0.005	[-0.14, 0.33]	4/6
Eastern Hemisphere	0.14	0.081	[-0.05, 0.44]	4/6	0.49	<0.001	[0.06, 0.58]	5/6
Western Hemisphere	0.18	<0.001	[-0.02, 0.54]	4/6	-0.28	<0.001	[-0.55, 0.07]	3/6
East–West Dipole	-0.04	0.688	[-0.11, 0.01]	4/6	0.77	0.002	[0.14, 1.03]	6/6

	G6solar-ssp585				G6sulfur-ssp585			
	Δ Thaw Depth	*P*-value	Bootstrap 95% CI	M.A.	Δ Thaw Depth	*P*-value	Bootstrap 95% CI	M.A.
Northern High Latitudes	-4.60	<0.001	[-4.77, -0.65]	5/6	-4.57	<0.001	[-5.31, -0.49]	5/6
Eastern Hemisphere	-5.16	<0.001	[-4.84, -0.72]	5/6	-4.81	<0.001	[-4.73, -0.51]	5/6
Western Hemisphere	-3.73	<0.001	[-5.92, -0.44]	5/6	-4.19	0.001	[-6.95, -0.48]	5/6

Figure 2. Difference in thaw depth under SAI. **(a)** Difference in mean summer (JJA) thaw depth (m) over the period 2080–2099 between G6solar-ssp245, G6sulfur-ssp245, G6solar-ssp585, and G6sulfur-ssp585. The black line represents areas with ≥ 50 % permafrost probability based on mean annual air temperature (MAAT) projections for the period 2080–2099 under ssp245. **(b)** Difference in mean summer (JJA) thaw depth (m) over the period 2080–2099 between G6solar-ssp245, G6sulfur-ssp245, G6solar-ssp585, and G6sulfur-ssp585, based on the time-series analysis, shown for the Northern High Latitudes and its two subregions, the Eastern Hemisphere and the Western Hemisphere. For the ssp245 comparisons, the east-west dipole is additionally shown. The *P*-value from the autocorrelation-corrected paired *t*-test of the time-series analysis, the bootstrap 95 % confidence interval, and model agreement (M.A., i.e., the proportion of the six ESMs agreeing on the sign of the difference) from the paired model-based analysis (see Sect. 2.2) are also provided.

the Supplement) show both positive and negative correlations with SPTD within the same season, depending on the pressure levels of the predictors being examined. This underscores the complexity and dynamic nature of the involved atmospheric processes.

Our results suggest a tendency toward a shift in winter weather in the Eastern Hemisphere under G6sulfur compared to ssp245, with generally higher air temperature, wind speed, cloud cover, and precipitation, alongside lower sea level pressure (Fig. 4). In summer, the weather tends toward conditions with lower humidity, wind speed, reduced cloud cover, and precipitation. In addition to these shifts in means, the results also show a wider range of values under G6sulfur than under ssp245, indicating more variable – and potentially more extreme – conditions. Overall, the G6sulfur anomaly forcing tends toward winter and summer conditions that are both less favorable for permafrost preservation across the Eastern Hemisphere. These results represent multi-model means, and individual months and models may show varying degrees of agreement.

The variance partitioning and correlation analysis for the Western Hemisphere show a different picture. Unlike in the Eastern Hemisphere, the explanatory power of these predictors (Fig. 5a and b) is very limited, with no single predictor exceeding an explained variance of 8.1 % in winter and 5.5 % in summer. In addition, the correlations (Fig. 5c and d) are weak, further indicating that SPTD drivers in this region are very similar in both scenarios, G6sulfur and ssp245.

Examining the variance partitioning analysis between the G6solar experiment and ssp245, the predictors show no divergence in the Eastern Hemisphere. This implies that the reduced permafrost protection potential in the Eastern Hemisphere under G6sulfur, compared to the ssp245 target scenario, is mainly influenced by the applied equatorial aerosol injection. In contrast, the variance partitioning analysis between the G6solar experiment and ssp245 show some alterations in the Western Hemisphere (Figs. S9 and S10 in the Supplement).

3.4 Influence of G6sulfur on large scale atmospheric patterns

Our variance partitioning analysis reveals that the change in winter zonal and meridional winds between G6sulfur and ssp245 is a key predictor in explaining the variation in summer permafrost thaw depth over the Eastern Hemisphere. Specifically, we observe a strengthening of stratospheric eastward winds under G6sulfur in the latitudes between 50 and 70° N, with a weakening of eastward flow below 50° N (Fig. 6b). These notable increases are particularly evident over the North Atlantic and the Bering Strait. Additionally, alterations in northward winds are observed, although less pronounced concerning windspeed (Fig. 6c). The difference in wind speed is notably more pronounced in the stratosphere than in the troposphere, as indicated by the data presented in Figs. S11–S14 in the Supplement. This effect is primarily evident under G6sulfur compared to ssp245 and nearly negligible under G6solar compared to ssp245. The spatial distribution of the wind speed anomaly shows increased northward flow in eastern Eurasia and reduced flow in western Eurasia under G6sulfur compared to ssp245 (Fig. 6c). This geographical pattern bears similarities to the changes in summer permafrost thaw depth observed across the Eastern Hemisphere and presented in Sect. 3.2.

The multi-model ensemble mean of sea level pressure shows a strong perturbation during boreal winter, characterized by a decrease in pressure north of 60° latitude with this negative difference intensifying towards the pole (Fig. 6a). Additionally, zones of high pressure develop around 50° N over the Atlantic Ocean and south of the Bering Strait. Changes over North America and Eurasia are comparatively less pronounced. A similar pressure configuration has been found by Jones et al. (2021) when comparing G6solar to G6sulfur using the CESM2-WACCM6 and UKESM1 models. They associated this pattern with a positive phase of the North Atlantic Oscillation (NAO). Subsequently, in a follow-up study, they found that G6sulfur consistently induces a progressively positive phase of the NAO during wintertime (Jones et al., 2022).

Our analysis reveals a significant strengthening of the winter (DJF) pressure gradient between the Azores and Iceland under G6sulfur compared to ssp245, with an increase of 6.30 hPa (± 3.35, P-value < 0.0001) and a NAO index increase of 1.02 (± 1.10, P-value < 0.0001, see Sect. 2.4 for the definition of the NAO index). While most pronounced in winter, the NAO is one of the few modes of variability that persists throughout the year (Linderholm and Folland, 2017). A positive (negative) summer NAO phase indicates a northward (southward) displacement of tropospheric jets and exerts notable surface climate effects (Dunstone et al., 2023). We observe no significant change in the summer pressure differential when comparing G6sulfur to ssp245 (Fig. 6e). However, the normalized NAO index shows a significant negative difference of -0.61 (± 0.60, P-value < 0.0001), indicating a weakening of the NAO during summer under G6sulfur (Fig. 6f).

In addition to the changes in pressure difference and normalized index induced by G6sulfur during winter and summer, the NAO correlates well with important predictors that explain the variance of summer permafrost thaw depth over the Eastern Hemisphere (Fig. 6d). This correlation, based on a 3-month rolling normalized average, is particularly strong for air temperature and the mass fraction of cloud ice, and to a lesser extent for the mass fraction of cloud liquid water. These interrelations weaken with increasing eastward longitude. Our results suggest, that G6sulfur is creating a large-scale atmospheric pattern change with a positive NAO index in winter and negative in summer influencing the SPTD, compared to ssp245, by altering the eastward air mass transport from the Atlantic Ocean over the Eurasian continent,

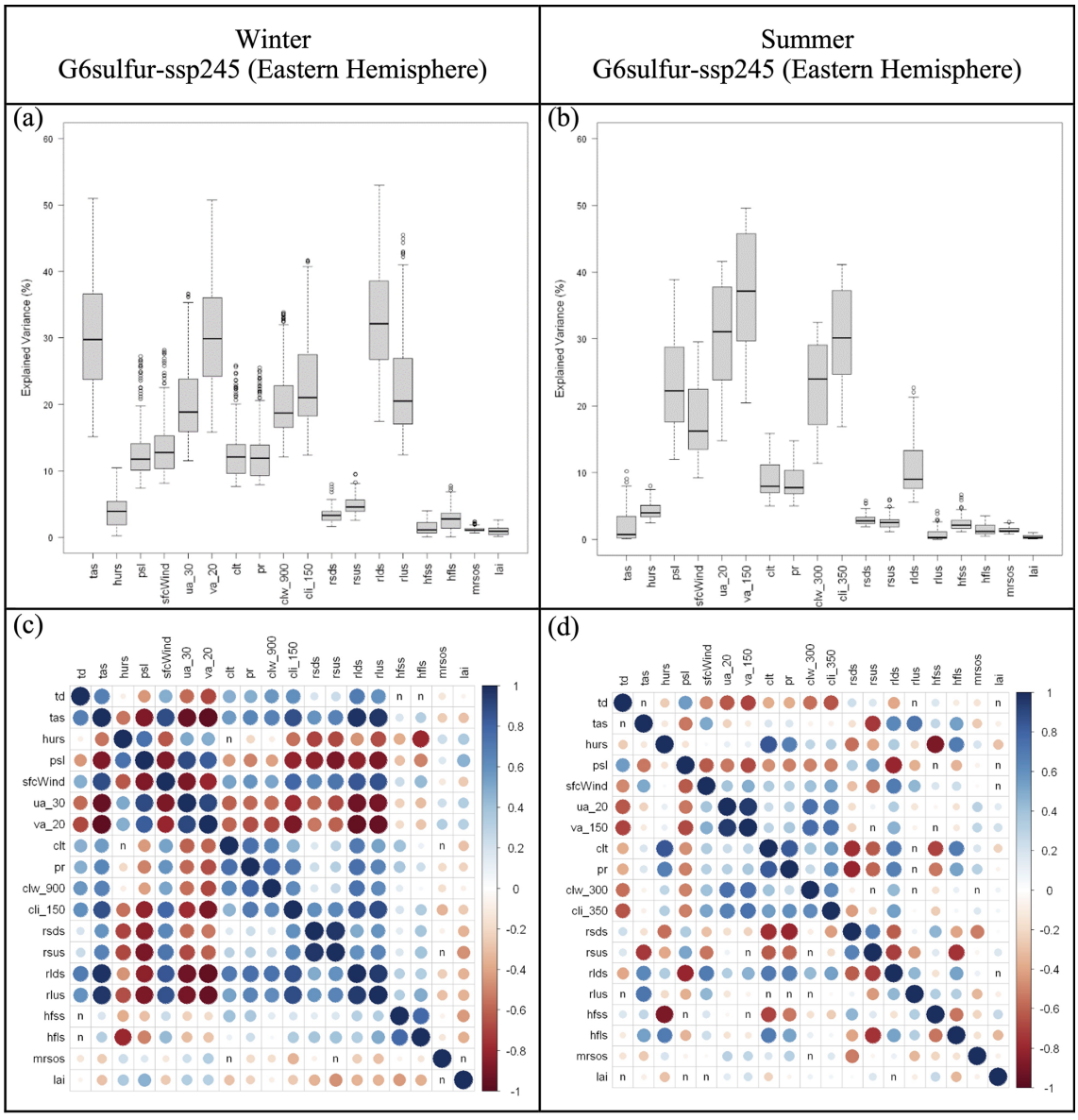

Figure 3. Influence of G6sulfur on SPTD drivers in the Eastern Hemisphere, derived from the G6sulfur-ssp245 difference. Top row: Average explained variance (%) in summer permafrost thaw depth by predictor and season for the difference G6sulfur-ssp245 across the Eastern Hemisphere, based on 3765 datapoints. Predictors are: tas (near-surface air temperature), hurs (near-surface relative humidity), psl (sea level pressure), sfcWind (near-surface wind speed), ua (eastward wind at specified hPa levels), va (northward wind at specified hPa levels), clt (total cloud cover percentage), pr (precipitation), clw (mass fraction of cloud liquid water at specified hPa levels), cli (mass fraction of cloud ice at specified hPa levels), rsds (surface downwelling shortwave radiation), rsus (surface upwelling shortwave radiation), rlds (surface downwelling longwave radiation), rlus (surface upwelling longwave radiation), hfss (surface upward sensible heat flux), hfls (surface upward latent heat flux), mrsos (moisture in upper portion of soil column), and lai (leaf area index). Panels: **(a)** winter (DJF), and **(b)** summer (JJA) predictors. Bottom row: Correlation matrix of the thaw depth (td) drivers by season, based on 3765 datapoints representing the difference between the G6sulfur experiment and the ssp245 scenario, with color indicating correlation direction (blue for positive, red for negative), and circle size indicating strength of correlation. Non-significant correlations are marked by "n". The first column shows the correlations between thaw depth (td) and each predictor and represents the primary focus of the correlation analysis discussed in the text; the remaining columns show correlations among the predictors and provide additional context for assessing potential multicollinearity. Panels: **(c)** winter (DJF), and **(d)** summer (JJA).

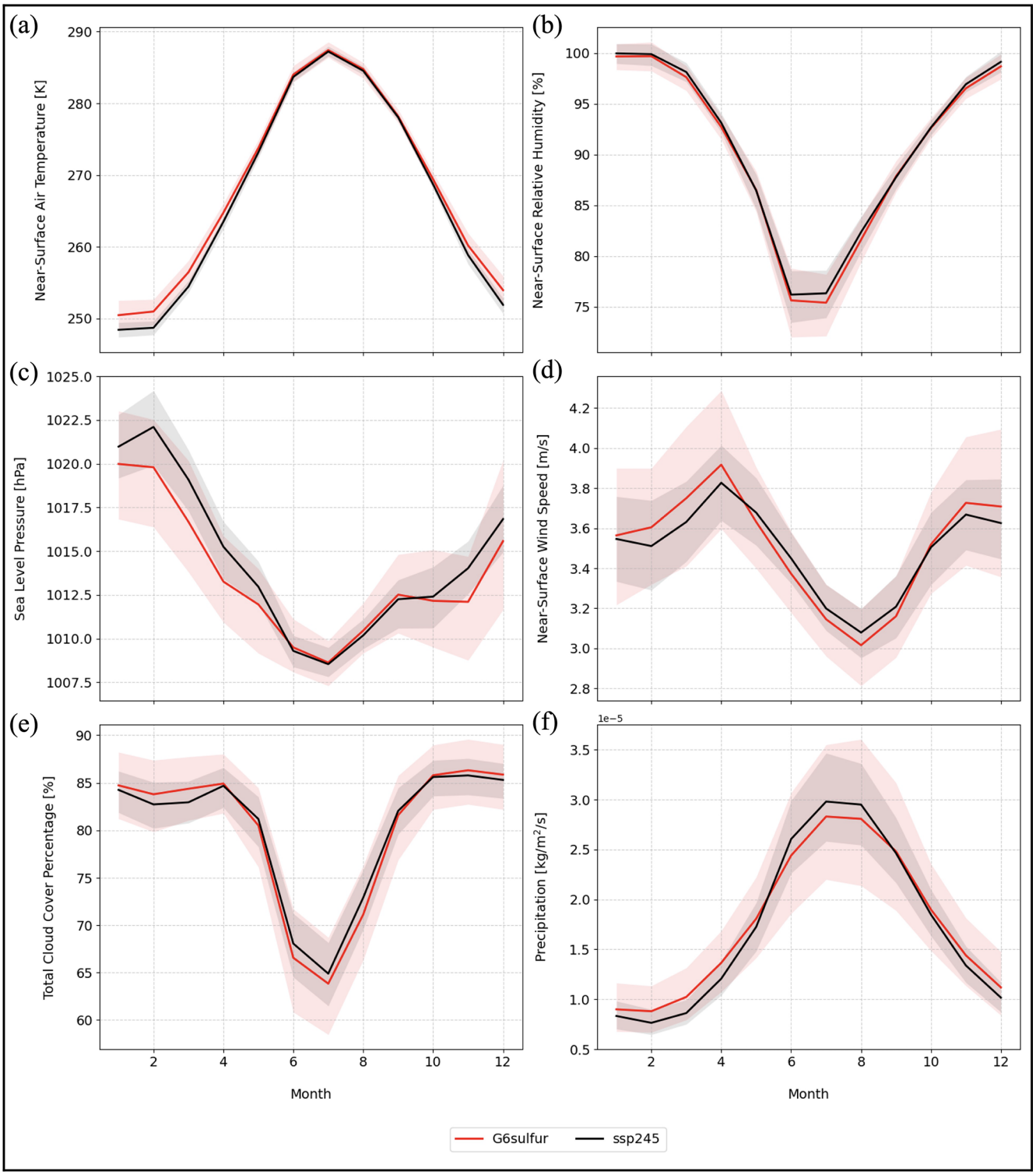

Figure 4. Monthly mean meteorological parameters in the Eastern Hemisphere (2080–2099). Panels show monthly mean values of key meteorological parameters over the period 2080–2099 under G6sulfur and ssp245: **(a)** near-surface air temperature, **(b)** near-surface relative humidity, **(c)** sea level pressure, **(d)** near-surface wind speed, **(e)** total cloud cover percentage, and **(f)** precipitation. Shaded areas indicate the maximum and minimum values for each parameter under the respective scenario.

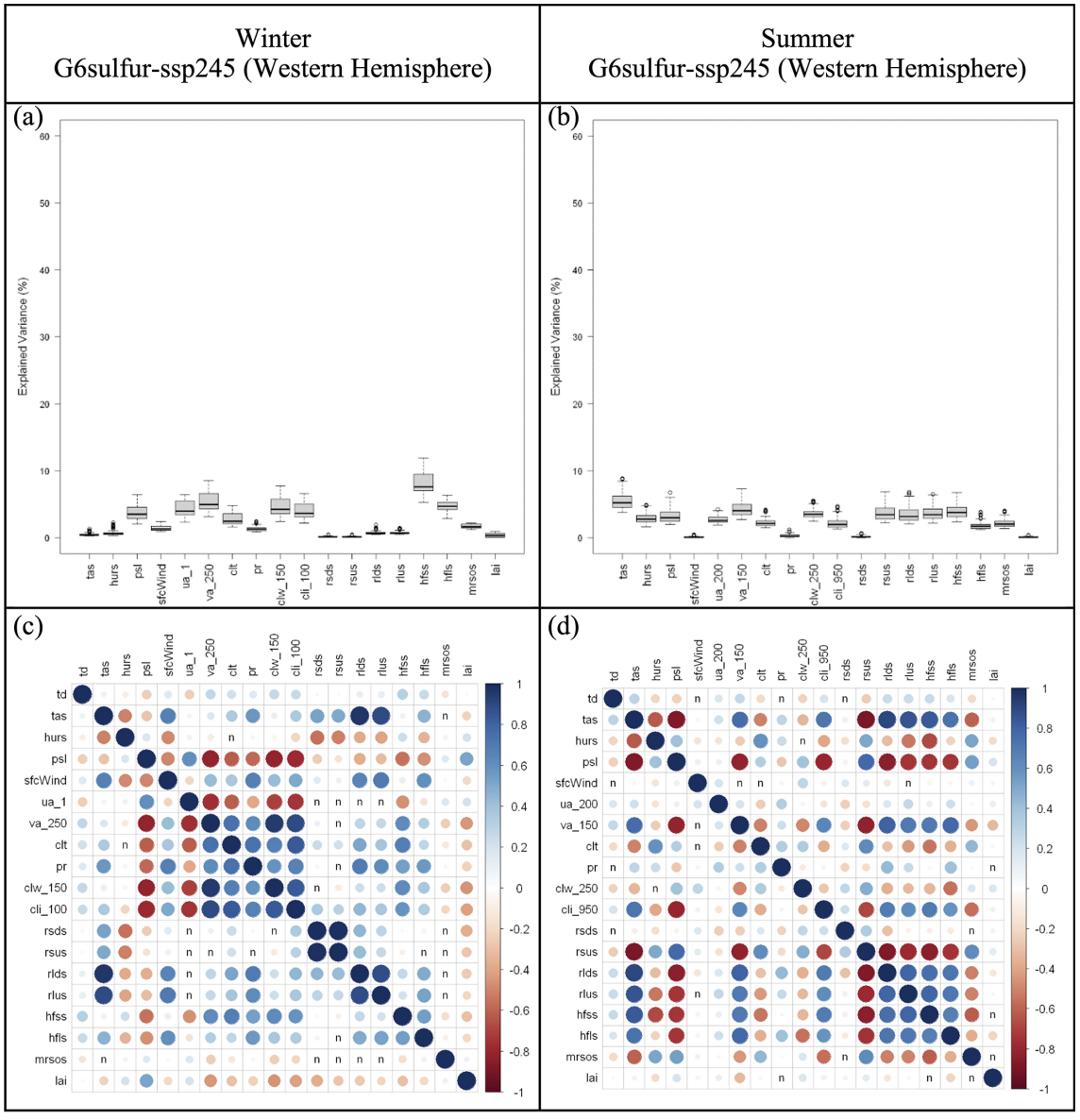

Figure 5. Influence of G6sulfur on SPTD drivers in the Western Hemisphere. Top row: Average explained variance (%) in summer permafrost thaw depth by predictor and season for the difference G6sulfur-ssp245 across the Western Hemisphere, based on 4000 datapoints. Predictors are: tas (near-surface air temperature), hurs (near-surface relative humidity), psl (sea level pressure), sfcWind (near-surface wind speed), ua (eastward wind at specified hPa levels), va (northward wind at specified hPa levels), clt (total cloud cover percentage), pr (precipitation), clw (mass fraction of cloud liquid water at specified hPa levels), cli (mass fraction of cloud ice at specified hPa levels), rsds (surface downwelling shortwave radiation), rsus (surface upwelling shortwave radiation), rlds (surface downwelling longwave radiation), rlus (surface upwelling longwave radiation), hfss (surface upward sensible heat flux), hfls (surface upward latent heat flux), mrsos (moisture in upper portion of soil column), and lai (leaf area index). Panels: **(a)** winter (DJF), and **(b)** summer (JJA) predictors. Bottom row: Correlation matrix of the thaw depth (td) drivers by season, based on 4000 datapoints, with color indicating correlation direction (blue for positive, red for negative), and circle size indicating strength of correlation. Non-significant correlations are marked by "n". The first column shows the correlations between thaw depth (td) and each predictor and represents the primary focus of the correlation analysis discussed in the text; the remaining columns show correlations among the predictors and provide additional context for assessing potential multicollinearity. Panels: **(c)** winter (DJF), and **(d)** summer (JJA).

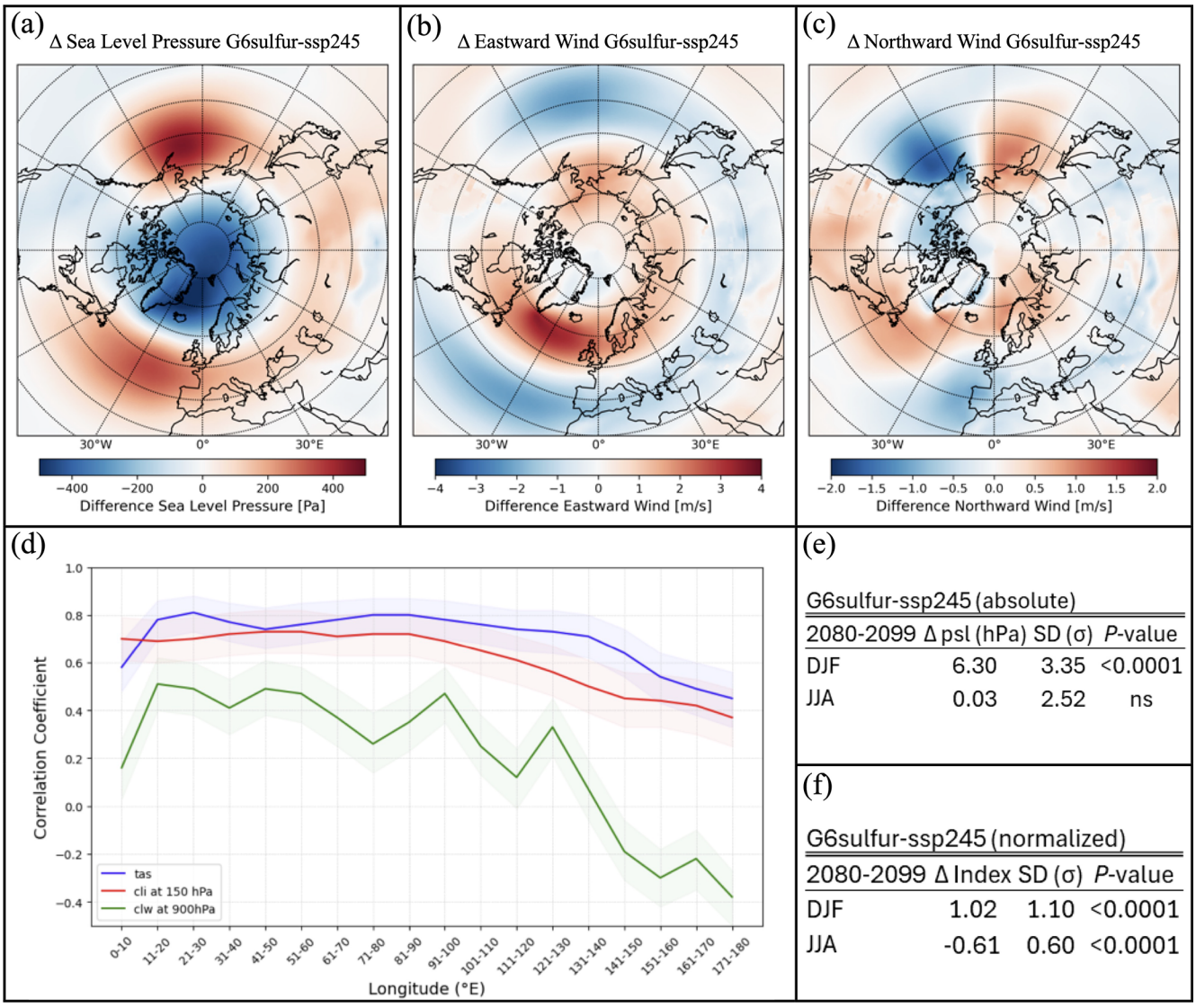

Figure 6. Influence of G6sulfur on large scale atmospheric patterns. **(a)** Difference in mean winter (DJF) sea level pressure over the period 2080–2099 between G6sulfur-ssp245. **(b)** Difference in mean winter (DJF) eastward wind at 850 hPa over the period 2080–2099 between G6sulfur-ssp245. **(c)** Difference in mean winter (DJF) northward wind at 850 hPa over the period 2080–2099 between G6sulfur-ssp245. **(d)** Correlation of North Atlantic Oscillation index with tas (near-surface air temperature), cli (mass fraction of cloud ice at 150 hPa), and clw (mass fraction of cloud liquid water at 900 hPa) across longitude segments between 65 and 75° N over the period 2080–2099, based on the G6sulfur-ssp245 difference. Shaded areas indicate the 95 % confidence interval. **(e)** Absolute difference in sea level pressure between the Azores and Iceland during winter (DJF) and summer (JJA) for the period 2080–2099, with "ns" indicating non-significant values. **(f)** Normalized difference in sea level pressure between the Azores and Iceland during winter (DJF) and summer (JJA) for the period 2080–2099.

modifying its effect with increasing longitude as the air travels over land and changes its physical properties. This NAO-driven mechanism provides a physically consistent explanation for the robust east–west dipole in summer permafrost thaw depth observed across all six ESMs.

4 Discussion

Our study shows that permafrost area is declining more rapidly (-1.08×10^6 km^2, P-value < 0.001) and the summer permafrost thaw depth is deeper (+0.190 m, P-value < 0.01) under G6sulfur compared to ssp245 during the period 2080–2099. A comparable finding, albeit using a different pathway as the control, was published by Müller et al. (2024). They reported that Arctic land with temperatures below freezing

is projected to decline by 7.8 % by the end of the century under SAI compared to RCP4.5. On the other hand, our study also shows that permafrost area is better preserved ($+4.61 \times 10^6$ km^2, P-value < 0.001) and the summer permafrost thaw depth is shallower (-4.57 m, P-value < 0.001) under G6sulfur compared to ssp585, which represents a business-as-usual scenario.

Furthermore, our study reveals a notable spatial divergence in the G6sulfur-ssp245 difference: in the Eastern Hemisphere, there is a pronounced retreat of permafrost area along with deeper summer permafrost thaw depths, whereas the Western Hemisphere shows a slight increase in permafrost area accompanied by a shallower, though less model-consistent, summer permafrost thaw depth response. The observed increase in permafrost decline in Western Siberia under G6sulfur, as highlighted in our study, is particularly significant. Grysko et al. (2024) noted that this region already experiences the strongest positive spring temperature trend in the Arctic, exceeding 1 °C per decade, and the strength has risen for heat extremes and declined for cold extremes. This implies a pre-existing warming pattern attributed to rising CO_2 emissions, which cannot be fully reduced by the G6sulfur scenario down to the targeted ssp245 warming level. There may be an underlying mechanism driven by the CO_2 content in the atmosphere connecting these observations, meriting additional investigation.

The regional difference in permafrost extent and summer permafrost thaw depth is accompanied by an evident shift in the relative significance of various permafrost drivers in the Eastern Arctic. In the Western Arctic, the importance of different summer permafrost thaw drivers remains relatively similar to ssp245. In the Eastern Hemisphere, the differences in predictive ability of the different drivers for summer permafrost thaw depth between G6sulfur and ssp245 show that the largest variations are observed in atmospheric variables such as zonal and meridional winds, cloud water and ice content, and the NAO in both winter and summer, thereby influencing temperature variations as well as the reflection and absorption of longwave radiation. This implies that SAI under the G6sulfur scenario causes substantial alterations in atmospheric circulation patterns at high latitudes during both boreal winter and summer. Previous studies by Banerjee et al. (2021) and Chen et al. (2023) have documented a residual winter warming phenomenon at high latitudes under SAI, resulting in increased temperatures during the boreal winter. Furthermore, research by Jones et al. (2021) showed a positive anomaly in the NAO during the winter season in the Northern Hemisphere under the G6sulfur scenario, indicating intensified zonal flow and enhanced North Atlantic storm track activity. These changes have implications for the Eastern Hemisphere, leading to high latitude warming over Europe and Asia. Similar effects have been observed with stratospheric volcanic aerosols resulting from volcanic eruptions in the tropics (Shindell et al., 2004), indicating that the changes produced by the models under G6sulfur are likely to be solid. While these studies established the large-scale atmospheric context, none quantified which specific drivers are responsible for the resulting permafrost thaw depth response. Our variance partitioning reveals that atmospheric circulation variables and cloud microphysical properties – rather than the shortwave radiation reduction that SAI is designed to achieve – are the dominant drivers of permafrost thaw depth differences between G6sulfur and ssp245.

The results of our study provide further support for the observed phenomena, revealing a pronounced sea level pressure gradient from the Azores to Iceland during boreal winter under G6sulfur. This suggests a shift towards a more positive NAO and an important intensification of the eastward wind pattern at 850 hPa, particularly above 50° N across all longitudes. Additionally, we observe a shift to a more negative NAO under G6sulfur during summer. These changes in strength and direction of the NAO show a strong correlation with air temperature, as well as the mass fraction of cloud ice, and to a lesser extent, the mass fraction of cloud liquid water over the Eastern Arctic. The correlations weaken with increasing longitude across the Eurasian continent.

The interactions between cloud properties as well as zonal and meridional winds on different pressure levels present a complex interplay that influences permafrost thaw dynamics. We have identified a positive correlation between cloud cover, the mass fraction of cloud liquid water and ice during wintertime and the summer thaw depth of permafrost. This suggests that clouds enhance summer permafrost thaw depths, likely due to the reflection of upwelling longwave radiation by ice crystals and water droplets, creating a longwave trapping effect during wintertime. This observation of increased downwelling longwave radiation is consistent with findings from Boisvert and Stroeve (2015) and Shupe and Intrieri (2004). Conversely, during summertime, a negative correlation is observed between cloud cover as well as the mass fraction of cloud liquid water and ice and summer permafrost thaw depth across various pressure levels, indicating a protective effect of clouds during this season. The varying strengths of this negative correlation highlight the complex nature of cloud-permafrost interactions. This protective effect during summer may be attributed to the reflection of sunlight by cloud layers back into space. These findings align with Alkama et al. (2020), who reported a 47 % overall damping effect of clouds on Arctic sea ice decline.

It is reasonable to assume that the implementation of G6sulfur induces a significant alteration in large-scale atmospheric patterns, particularly characterized by an amplification of the NAO during boreal winter. This phenomenon results in a heightened eastward flow of moist and warmer air masses originating from the Atlantic Ocean, thereby contributing to elevated temperatures and increased cloud cover over the Eurasian region. The intensified cloud cover, potentially containing higher concentrations of liquid water or ice particles, acts as an effective barrier to the escape of upwelling longwave radiation into space. This, combined with

higher temperatures, contributes to an increased retention of heat within the atmosphere. As a result, a considerable portion of the longwave radiation is reflected back towards the Earth's surface, effectively creating a mechanism akin to a longwave trapping effect. These combined atmospheric changes lead to elevated temperatures and enhanced energy fluxes at the surface, ultimately contributing to an increased summer permafrost thaw depth over the high latitude Eastern Hemisphere. As the air mass moves further over Eurasia, the effectiveness of this mechanism may diminish. The air mass tends to dry up and cool as it traverses over land, leading to a reduction in moisture content and thermal properties. Consequently, the intensity of the longwave trapping effect diminishes, and the associated increase in summer permafrost thaw depth may be less pronounced, particularly over inland regions or after mountain ridges where the air mass has undergone significant drying and cooling processes.

Whereas boreal winter is marked by a positive NAO, G6sulfur induces a more negative NAO during boreal summer compared to ssp245. It can be hypothesized that there is a decrease in zonal flow and fewer humid air masses arriving from the Atlantic Ocean. This could create a weather pattern more favorable for reducing permafrost thaw, with lower humidity, reduced wind speed, diminished cloud cover, and decreased precipitation. However, this scenario may also pose potential drawbacks, as the land surface becomes less protected by clouds, resulting in less reflection of incoming shortwave radiation by clouds back into space and therefore negatively impacting the summer permafrost thaw depth.

Summer shortwave energy fluxes seem to have very limited predictive power in explaining the difference in summer permafrost thaw depth between G6sulfur and ssp245. Although net shortwave radiation decreases over the Eastern Arctic during boreal summer under G6sulfur, this change does not significantly contribute to the observed thaw depth differences. This observation appears counterintuitive, considering that SAI is designed to reduce incoming solar radiation. This raises the question of whether an alternative injection strategy – one targeting regions closer to the poles, with a higher concentration of SO_2 and consequently greater aerosol optical depth at high latitudes – would yield different outcomes, compared to the equatorial injection implemented in the GEOMIP6 G6sulfur experiment analyzed in this study.

It is crucial to acknowledge the inherent variability in model response of the six ESMs used in this study. Visioni et al. (2021) found that, across the final two decades of the century, significant disparities emerge among models in terms of required sulphate injection amounts ($29 \pm 9\,\mathrm{Tg\,SO_2\,yr^{-1}}$ between 2081 and 2100), the latitudinal distribution of the aerosol cloud, and resultant stratospheric temperature changes. Even within the simpler G6solar experiment, there is variation in the level of solar dimming necessary to achieve the same global temperature target. This highlights the necessity of further improving and refining the model techniques, particularly crucial for accurately representing complex phenomena like permafrost freeze-thaw dynamics.

5 Conclusions

In conclusion, the G6sulfur experiment aims to bring global mean near-surface air temperatures from ssp585 toward ssp245 levels by introducing stratospheric aerosols along a single equatorial longitude band from 10° S to 10° N. While achieving the targeted temperature response, the G6sulfur experiment induces a large-scale atmospheric pattern change, accelerating the decline of total high-latitude permafrost area compared to ssp245 and producing a robust east–west dipole in summer permafrost thaw depth: deeper thaw in the Eastern Arctic and a shallower, though less model-consistent, response in the Western Arctic. Our study explores the mechanisms behind these changes and seeks to understand why G6sulfur, despite better preserving permafrost compared to ssp585, does not preserve permafrost to the same extent as ssp245, even though it is designed to achieve a similar global mean near-surface air temperature. This divergence highlights the complex interactions between geoengineering interventions and Earth system processes.

Although the coordinated GeoMIP6 experiments outlined in this study provide valuable insights, it is essential to acknowledge that they represent only one approach to SAI deployment and may not be the most optimal (Visioni et al., 2021). The impacts of SAI largely depend on the spatial and temporal patterns of aerosol optical depth. This opens a variety of strategic injection choices regarding season, location, quantity, and altitude. Visioni et al. (2019) suggest that injecting aerosols throughout the year may not be optimal, as seasonal distribution could significantly impact climatic effects. Kravitz et al. (2019) and Macmartin et al. (2017) demonstrate that alternative approaches, like dispersing aerosols at different locations beyond low latitudes, could offer better control over the spatial distribution of aerosol optical depth. This potentially leads to enhanced results by more effectively regulating global mean temperatures, interhemispheric gradients, and temperature variations from the equator to the poles. Furthermore, Lee et al. (2023) investigated high-latitude injection strategies at 60° N concentrated over the months of March, April, and May. They found that such strategies have a more pronounced impact on cooling at the pole compared to a globally focused SAI strategy that injects similar quantities of SO_2, thereby reducing the large-scale climate pattern changes induced by SAI at lower latitudes. Studying the impact of different injection strategies on the drivers influencing summer permafrost thaw depth emerges as an important area for future research. Through these investigations, we gain valuable insights into the factors affecting permafrost dynamics and improve our understanding of the potential efficacy and consequences of various SAI strategies.

Code and data availability. The code used for the extraction and analysis of GEOMIP model output, statistical analysis, variance partitioning analysis, and plotting the figures is openly available on GitHub via: https://doi.org/10.5281/zenodo.18131432 (Businger, 2026a). The data that support this study were extracted from the GEOMIP data download location https://aims2.llnl.gov/search (last access: 15 October 2025), permafrost area and thaw depth data derived from the GEOMIP data can be found on Zenodo: https://doi.org/10.5281/zenodo.18100787 (Businger, 2026b).

Supplement. The supplement related to this article is available online at https://doi.org/10.5194/esd-17-1779-2026-supplement.

Author contributions. IB conceptualized the study, performed the analysis, and prepared the manuscript. RM and RG provided scientific input and reviewed the manuscript. JO contributed to the analysis of a specific component of the study, provided relevant code for this component, and reviewed the manuscript. JK reviewed the manuscript. GSS supervised the work, provided scientific guidance, and contributed to the revision of the manuscript. All authors reviewed and approved the final manuscript.

Competing interests. The contact author has declared that none of the authors has any competing interests.

Disclaimer. Publisher's note: Copernicus Publications remains neutral with regard to jurisdictional claims made in the text, published maps, institutional affiliations, or any other geographical representation in this paper. The authors bear the ultimate responsibility for providing appropriate place names. Views expressed in the text are those of the authors and do not necessarily reflect the views of the publisher.

Acknowledgements. We would like to thank the GEOMIP project members for providing geoengineering simulations.

Financial support. Jin-Soo Kim was supported by the KAIST Startup Grant (G04250056).

Review statement. This paper was edited by Ben Kravitz and reviewed by two anonymous referees.

References

ACGR: Glossary of permafrost and related ground-ice terms, https://doi.org/10.4224/20386561, 1988.

Alkama, R., Taylor, P. C., Garcia-San Martin, L., Douville, H., Duveiller, G., Forzieri, G., Swingedouw, D., and Cescatti, A.: Clouds damp the radiative impacts of polar sea ice loss, The Cryosphere, 14, 2673–2686, https://doi.org/10.5194/tc-14-2673-2020, 2020.

Armstrong McKay, D. I., Staal, A., Abrams, J. F., Winkelmann, R., Sakschewski, B., Loriani, S., Fetzer, I., Cornell, S. E., Rockström, J., and Lenton, T. M.: Exceeding 1.5 °C global warming could trigger multiple climate tipping points, Science, 377, https://doi.org/10.1126/science.abn7950, 2022.

Banerjee, A., Butler, A. H., Polvani, L. M., Robock, A., Simpson, I. R., and Sun, L.: Robust winter warming over Eurasia under stratospheric sulfate geoengineering – the role of stratospheric dynamics, Atmos. Chem. Phys., 21, 6985–6997, https://doi.org/10.5194/acp-21-6985-2021, 2021.

Biskaborn, B. K., Smith, S. L., Noetzli, J., Matthes, H., Vieira, G., Streletskiy, D. A., Schoeneich, P., Romanovsky, V. E., Lewkowicz, A. G., Abramov, A., Allard, M., Boike, J., Cable, W. L., Christiansen, H. H., Delaloye, R., Diekmann, B., Drozdov, D., Etzelmüller, B., Grosse, G., Guglielmin, M., Ingeman-Nielsen, T., Isaksen, K., Ishikawa, M., Johansson, M., Johannsson, H., Joo, A., Kaverin, D., Kholodov, A., Konstantinov, P., Kröger, T., Lambiel, C., Lanckman, J. P., Luo, D., Malkova, G., Meiklejohn, I., Moskalenko, N., Oliva, M., Phillips, M., Ramos, M., Sannel, A. B. K., Sergeev, D., Seybold, C., Skryabin, P., Vasiliev, A., Wu, Q., Yoshikawa, K., Zheleznyak, M., and Lantuit, H.: Permafrost is warming at a global scale, Nat. Commun., 10, https://doi.org/10.1038/s41467-018-08240-4, 2019.

Boisvert, L. N. and Stroeve, J. C.: The Arctic is becoming warmer and wetter as revealed by the Atmospheric Infrared Sounder, Geophys. Res. Lett., 42, 4439–4446, https://doi.org/10.1002/2015GL063775, 2015.

Boucher, O., Servonnat, J., Albright, A. L., Aumont, O., Balkanski, Y., Bastrikov, V., Bekki, S., Bonnet, R., Bony, S., Bopp, L., Braconnot, P., Brockmann, P., Cadule, P., Caubel, A., Cheruy, F., Codron, F., Cozic, A., Cugnet, D., D'Andrea, F., Davini, P., de Lavergne, C., Denvil, S., Deshayes, J., Devilliers, M., Ducharne, A., Dufresne, J.-L., Dupont, E., Éthé, C., Fairhead, L., Falletti, L., Flavoni, S., Foujols, M.-A., Gardoll, S., Gastineau, G., Ghattas, J., Grandpeix, J.-Y., Guenet, B., Guez, L. E., Guilyardi, E., Guimberteau, M., Hauglustaine, D., Hourdin, F., Idelkadi, A., Joussaume, S., Kageyama, M., Khodri, M., Krinner, G., Lebas, N., Levavasseur, G., Lévy, C., Li, L., Lott, F., Lurton, T., Luyssaert, S., Madec, G., Madeleine, J.-B., Maignan, F., Marchand, M., Marti, O., Mellul, L., Meurdesoif, Y., Mignot, J., Musat, I., Ottlé, C., Peylin, P., Planton, Y., Polcher, J., Rio, C., Rochetin, N., Rousset, C., Sepulchre, P., Sima, A., Swingedouw, D., Thiéblemont, R., Traore, A. K., Vancoppenolle, M., Vial, J., Vialard, J., Viovy, N., and Vuichard, N.: Presentation and Evaluation of the IPSL-CM6A-LR Climate Model, J. Adv. Model. Earth Sy., 12, e2019MS002010, https://doi.org/10.1029/2019MS002010, 2020.

Burke, E. J., Zhang, Y., and Krinner, G.: Evaluating permafrost physics in the Coupled Model Intercomparison Project 6 (CMIP6) models and their sensitivity to climate change, The Cryosphere, 14, 3155–3174, https://doi.org/10.5194/tc-14-3155-2020, 2020.

Businger, I.: ibusinger/PermafrostUnderSAI: v1.0.0, Zenodo [software], https://doi.org/10.5281/zenodo.18131432, 2026a.

Businger, I.: Permafrost area and thaw depth data, Zenodo [data set], https://doi.org/10.5281/zenodo.18100787, 2026b.

Chadburn, S. E., Burke, E. J., Essery, R. L. H., Boike, J., Langer, M., Heikenfeld, M., Cox, P. M., and Friedlingstein, P.: Impact of model developments on present and future simulations of permafrost in a global land-surface model, The Cryosphere, 9, 1505–1521, https://doi.org/10.5194/tc-9-1505-2015, 2015.

Chadburn, S. E., Burke, E. J., Cox, P. M., Friedlingstein, P., Hugelius, G., and Westermann, S.: An observation-based constraint on permafrost loss as a function of global warming, Nat. Clim. Change, 7, 340–344, https://doi.org/10.1038/nclimate3262, 2017.

Chen, Y., Liu, A., and Moore, J. C.: Mitigation of Arctic permafrost carbon loss through stratospheric aerosol geoengineering, Nat. Commun., 11, https://doi.org/10.1038/s41467-020-16357-8, 2020.

Chen, Y., Ji, D., Zhang, Q., Moore, J. C., Boucher, O., Jones, A., Lurton, T., Mills, M. J., Niemeier, U., Séférian, R., and Tilmes, S.: Northern-high-latitude permafrost and terrestrial carbon response to two solar geoengineering scenarios, Earth Syst. Dynam., 14, 55–79, https://doi.org/10.5194/esd-14-55-2023, 2023.

Crutzen, P. J.: Albedo enhancement by stratospheric sulfur injections: A contribution to resolve a policy dilemma?, Climatic Change, 77, https://doi.org/10.1007/s10584-006-9101-y, 2006.

Danabasoglu, G., Lamarque, J.-F., Bacmeister, J., Bailey, D. A., DuVivier, A. K., Edwards, J., Emmons, L. K., Fasullo, J., Garcia, R., Gettelman, A., Hannay, C., Holland, M. M., Large, W. G., Lauritzen, P. H., Lawrence, D. M., Lenaerts, J. T. M., Lindsay, K., Lipscomb, W. H., Mills, M. J., Neale, R., Oleson, K. W., Otto-Bliesner, B., Phillips, A. S., Sacks, W., Tilmes, S., van Kampenhout, L., Vertenstein, M., Bertini, A., Dennis, J., Deser, C., Fischer, C., Fox-Kemper, B., Kay, J. E., Kinnison, D., Kushner, P. J., Larson, V. E., Long, M. C., Mickelson, S., Moore, J. K., Nienhouse, E., Polvani, L., Rasch, P. J., and Strand, W. G.: The Community Earth System Model Version 2 (CESM2), J. Adv. Model. Earth Sy., 12, e2019MS001916, https://doi.org/10.1029/2019MS001916, 2020.

Dunstone, N., Smith, D. M., Hardiman, S. C., Hermanson, L., Ineson, S., Kay, G., Li, C., Lockwood, J. F., Scaife, A. A., Thornton, H., Ting, M., and Wang, L.: Skilful predictions of the Summer North Atlantic Oscillation, Commun. Earth Environ., 4, https://doi.org/10.1038/s43247-023-01063-2, 2023.

Eugster, W., Rouse, W. R., Pielke, R. A., Mcfadden, J. P., Baldocchi, D. D., Kittel, T. G. F., Chapin, F. S., Liston, G. E., Vidale, P. L., Vaganov, E., and Chambers, S.: Land-atmosphere energy exchange in Arctic tundra and boreal forest: Available data and feedbacks to climate, Glob. Chang. Biol., 6, 84–115, https://doi.org/10.1046/j.1365-2486.2000.06015.x, 2000.

Gallet, J.-C., Domine, F., Arnaud, L., Picard, G., and Savarino, J.: Vertical profile of the specific surface area and density of the snow at Dome C and on a transect to Dumont D'Urville, Antarctica – albedo calculations and comparison to remote sensing products, The Cryosphere, 5, 631–649, https://doi.org/10.5194/tc-5-631-2011, 2011.

Garnello, A., Marchenko, S., Nicolsky, D., Romanovsky, V., Ledman, J., Celis, G., Schädel, C., Luo, Y., and Schuur, E. A. G.: Projecting Permafrost Thaw of Sub-Arctic Tundra With a Thermodynamic Model Calibrated to Site Measurements, J. Geophys. Res.-Biogeo., 126, https://doi.org/10.1029/2020JG006218, 2021.

Gettelman, A., Hannay, C., Bacmeister, J. T., Neale, R. B., Pendergrass, A. G., Danabasoglu, G., Lamarque, J.-F., Fasullo, J. T., Bailey, D. A., Lawrence, D. M., and Mills, M. J.: High Climate Sensitivity in the Community Earth System Model Version 2 (CESM2), Geophys. Res. Lett., 46, 8329–8337, https://doi.org/10.1029/2019GL083978, 2019.

Grömping, U.: Relative Importance for Linear Regression in R: The Package relaimpo, J. Stat. Softw., 17, 1–27, https://doi.org/10.18637/jss.v017.i01, 2006.

Gruber, S.: Derivation and analysis of a high-resolution estimate of global permafrost zonation, The Cryosphere, 6, 221–233, https://doi.org/10.5194/tc-6-221-2012, 2012.

Grysko, R., Kim, J. S., and Schaepman-Strub, G.: Arctic springtime temperature and energy flux interannual variability is driven by 1- to 2-week frequency atmospheric events, Weather Clim. Extrem., 43, https://doi.org/10.1016/j.wace.2024.100650, 2024.

Hugelius, G., Strauss, J., Zubrzycki, S., Harden, J. W., Schuur, E. A. G., Ping, C.-L., Schirrmeister, L., Grosse, G., Michaelson, G. J., Koven, C. D., O'Donnell, J. A., Elberling, B., Mishra, U., Camill, P., Yu, Z., Palmtag, J., and Kuhry, P.: Estimated stocks of circumpolar permafrost carbon with quantified uncertainty ranges and identified data gaps, Biogeosciences, 11, 6573–6593, https://doi.org/10.5194/bg-11-6573-2014, 2014.

IPCC: Global Warming of 1.5 °C, Cambridge University Press, https://doi.org/10.1017/9781009157940, 2022.

Jiang, J., Cao, L., MacMartin, D. G., Simpson, I. R., Kravitz, B., Cheng, W., Visioni, D., Tilmes, S., Richter, J. H., and Mills, M. J.: Stratospheric Sulfate Aerosol Geoengineering Could Alter the High-Latitude Seasonal Cycle, Geophys. Res. Lett., 46, 14153–14163, https://doi.org/10.1029/2019GL085758, 2019.

Jones, A., Haywood, J. M., Jones, A. C., Tilmes, S., Kravitz, B., and Robock, A.: North Atlantic Oscillation response in GeoMIP experiments G6solar and G6sulfur: why detailed modelling is needed for understanding regional implications of solar radiation management, Atmos. Chem. Phys., 21, 1287–1304, https://doi.org/10.5194/acp-21-1287-2021, 2021.

Jones, A., Haywood, J. M., Scaife, A. A., Boucher, O., Henry, M., Kravitz, B., Lurton, T., Nabat, P., Niemeier, U., Séférian, R., Tilmes, S., and Visioni, D.: The impact of stratospheric aerosol intervention on the North Atlantic and Quasi-Biennial Oscillations in the Geoengineering Model Intercomparison Project (GeoMIP) G6sulfur experiment, Atmos. Chem. Phys., 22, 2999–3016, https://doi.org/10.5194/acp-22-2999-2022, 2022.

Kravitz, B., Robock, A., Tilmes, S., Boucher, O., English, J. M., Irvine, P. J., Jones, A., Lawrence, M. G., MacCracken, M., Muri, H., Moore, J. C., Niemeier, U., Phipps, S. J., Sillmann, J., Storelvmo, T., Wang, H., and Watanabe, S.: The Geoengineering Model Intercomparison Project Phase 6 (GeoMIP6): simulation design and preliminary results, Geosci. Model Dev., 8, 3379–3392, https://doi.org/10.5194/gmd-8-3379-2015, 2015.

Kravitz, B., MacMartin, D. G., Tilmes, S., Richter, J. H., Mills, M. J., Cheng, W., Dagon, K., Glanville, A. S., Lamarque, J. F., Simpson, I. R., Tribbia, J., and Vitt, F.: Comparing Surface and Stratospheric Impacts of Geoengineering With Different SO_2 Injection Strategies, J. Geophys. Res.-Atmos., 124, 7900–7918, https://doi.org/10.1029/2019JD030329, 2019.

Lee, H., Ekici, A., Tjiputra, J., Muri, H., Chadburn, S. E., Lawrence, D. M., and Schwinger, J.: The Response of Permafrost and High-Latitude Ecosystems Under Large-Scale Stratospheric Aerosol

Injection and Its Termination, Earth's Future, 7, 605–614, https://doi.org/10.1029/2018EF001146, 2019.

Lee, W. R., MacMartin, D. G., Visioni, D., Kravitz, B., Chen, Y., Moore, J. C., Leguy, G., Lawrence, D. M., and Bailey, D. A.: High-Latitude Stratospheric Aerosol Injection to Preserve the Arctic, Earth's Future, 11, https://doi.org/10.1029/2022EF003052, 2023.

Lindeman, R. H., Merenda, P. F., and Gold, R. Z.: Introduction to Bivariate and Multivariate Analysis, Glenview, Ill.: Scott, Foresman, https://archive.org/details/introductiontobi0000lind/page/n9/mode/2up (last access: 21 May 2025), 1980.

Linderholm, H. W. and Folland, C. K.: Summer North Atlantic Oscillation (SNAO) variability on decadal to palaeoclimate time scales, Past Global Changes Magazine, 25, 57–60, https://doi.org/10.22498/pages.25.1.57, 2017.

Liu, A., Moore, J. C., and Chen, Y.: PInc-PanTher estimates of Arctic permafrost soil carbon under the GeoMIP G6solar and G6sulfur experiments, Earth Syst. Dynam., 14, 39–53, https://doi.org/10.5194/esd-14-39-2023, 2023.

Lurton, T., Balkanski, Y., Bastrikov, V., Bekki, S., Bopp, L., Braconnot, P., Brockmann, P., Cadule, P., Contoux, C., Cozic, A., Cugnet, D., Dufresne, J.-L., Éthé, C., Foujols, M.-A., Ghattas, J., Hauglustaine, D., Hu, R.-M., Kageyama, M., Khodri, M., Lebas, N., Levavasseur, G., Marchand, M., Ottlé, C., Peylin, P., Sima, A., Szopa, S., Thiéblemont, R., Vuichard, N., and Boucher, O.: Implementation of the CMIP6 Forcing Data in the IPSL-CM6A-LR Model, J. Adv. Model. Earth Sy., 12, e2019MS001940, https://doi.org/10.1029/2019MS001940, 2020.

Macmartin, D. G., Kravitz, B., Tilmes, S., Richter, J. H., Mills, M. J., Lamarque, J. F., Tribbia, J. J., and Vitt, F.: The climate response to stratospheric aerosol geoengineering can be tailored using multiple injection locations, J. Geophys. Res.-Atmos., 122, 12,574-12,590, https://doi.org/10.1002/2017JD026868, 2017.

McGuire, A. D., Lawrence, D. M., Koven, C., Clein, J. S., Burke, E., Chen, G., Jafarov, E., MacDougall, A. H., Marchenko, S., Nicolsky, D., Peng, S., Rinke, A., Ciais, P., Gouttevin, G., Hayes, D. J., Ji, D., Krinner, G., Moore, J. C., Romanovsky, V., Schädel, C., Schaefer, K., Schuur, E. A. G., and Zhuang, Q.: Dependence of the evolution of carbon dynamics in the northern permafrost region on the trajectory of climate change, P. Natl. Acad. Sci. USA, 115, 3882–3887, https://doi.org/10.1073/pnas.1719903115, 2018.

Morrison, A. L., Barnes, E. A., and Hurrell, J. W.: Natural Variability Can Mask Forced Permafrost Response to Stratospheric Aerosol Injection in the ARISE-SAI-1.5 Simulations, Earth's Future, 12, https://doi.org/10.1029/2023EF004191, 2024a.

Morrison, A. L., Barnes, E. A., and Hurrell, J. W.: Stratospheric Aerosol Injection to Stabilize Northern Hemisphere Terrestrial Permafrost Under the ARISE-SAI-1.5 Scenario, Earth's Future, 12, https://doi.org/10.1029/2023EF004151, 2024b.

Müller, R. C., Kim, J. S., Lee, H., Muri, H., Tjiputra, J., Yoon, J. H., and Schaepman-Strub, G.: Radiative forcing geoengineering causes higher risk of wildfires and permafrost thawing over the Arctic regions, Commun. Earth Environ., 5, https://doi.org/10.1038/s43247-024-01329-3, 2024.

Muller, W. A., Jungclaus, J. H., Mauritsen, T., Baehr, J., Bittner, M., Budich, R., Bunzel, F., Esch, M., Ghosh, R., Haak, H., Ilyina, T., Kleine, T., Kornblueh, L., Li, H., Modali, K., Notz, D., Pohlmann, H., Roeckner, E., Stemmler, I., Tian, F., and Marotzke, J.: A Higher-resolution Version of the Max Planck Institute Earth System Model (MPI-ESM1.2-HR), J. Adv. Model. Earth Sy., 10, 1383–1413, https://doi.org/10.1029/2017MS001217, 2018.

Niemeier, U. and Schmidt, H.: Changing transport processes in the stratosphere by radiative heating of sulfate aerosols, Atmos. Chem. Phys., 17, 14871–14886, https://doi.org/10.5194/acp-17-14871-2017, 2017.

Niemeier, U., Richter, J. H., and Tilmes, S.: Differing responses of the quasi-biennial oscillation to artificial SO_2 injections in two global models, Atmos. Chem. Phys., 20, 8975–8987, https://doi.org/10.5194/acp-20-8975-2020, 2020.

Nitzbon, J., Schneider von Deimling, T., Aliyeva, M., Chadburn, S. E., Grosse, G., Laboor, S., Lee, H., Lohmann, G., Steinert, N. J., Stuenzi, S. M., Werner, M., Westermann, S., and Langer, M.: No respite from permafrost-thaw impacts in the absence of a global tipping point, Nat. Clim. Change, 14, 573–585, https://doi.org/10.1038/s41558-024-02011-4, 2024.

Obu, J.: How Much of the Earth's Surface is Underlain by Permafrost?, J. Geophys. Res. Earth Surf., 126, e2021JF006123, https://doi.org/10.1029/2021JF006123, 2021.

Oehri, J., Schaepman-Strub, G., Kim, J. S., Grysko, R., Kropp, H., Grünberg, I., Zemlianskii, V., Sonnentag, O., Euskirchen, E. S., Reji Chacko, M., Muscari, G., Blanken, P. D., Dean, J. F., di Sarra, A., Harding, R. J., Sobota, I., Kutzbach, L., Plekhanova, E., Riihelä, A., Boike, J., Miller, N. B., Beringer, J., López-Blanco, E., Stoy, P. C., Sullivan, R. C., Kejna, M., Parmentier, F. J. W., Gamon, J. A., Mastepanov, M., Wille, C., Jackowicz-Korczynski, M., Karger, D. N., Quinton, W. L., Putkonen, J., van As, D., Christensen, T. R., Hakuba, M. Z., Stone, R. S., Metzger, S., Vandecrux, B., Frost, G. V., Wild, M., Hansen, B., Meloni, D., Domine, F., te Beest, M., Sachs, T., Kalhori, A., Rocha, A. V., Williamson, S. N., Morris, S., Atchley, A. L., Essery, R., Runkle, B. R. K., Holl, D., Riihimaki, L. D., Iwata, H., Schuur, E. A. G., Cox, C. J., Grachev, A. A., McFadden, J. P., Fausto, R. S., Göckede, M., Ueyama, M., Pirk, N., de Boer, G., Bret-Harte, M. S., Leppäranta, M., Steffen, K., Friborg, T., Ohmura, A., Edgar, C. W., Olofsson, J., and Chambers, S. D.: Vegetation type is an important predictor of the arctic summer land surface energy budget, Nat. Commun., 13, https://doi.org/10.1038/s41467-022-34049-3, 2022.

Ohta, T., Maximov, T. C., Dolman, A. J., Nakai, T., van der Molen, M. K., Kononov, A. V., Maximov, A. P., Hiyama, T., Iijima, Y., Moors, E. J., Tanaka, H., Toba, T., and Yabuki, H.: Interannual variation of water balance and summer evapotranspiration in an eastern Siberian larch forest over a 7-year period (1998–2006), Agric. For. Meteorol., 148, 1941–1953, https://doi.org/10.1016/j.agrformet.2008.04.012, 2008.

O'Neill, B. C., Kriegler, E., Ebi, K. L., Kemp-Benedict, E., Riahi, K., Rothman, D. S., van Ruijven, B. J., van Vuuren, D. P., Birkmann, J., Kok, K., Levy, M., and Solecki, W.: The roads ahead: Narratives for shared socioeconomic pathways describing world futures in the 21st century, Global Environmental Change, 42, 169–180, https://doi.org/10.1016/j.gloenvcha.2015.01.004, 2017.

Rantanen, M., Karpechko, A. Y., Lipponen, A., Nordling, K., Hyvärinen, O., Ruosteenoja, K., Vihma, T., and Laaksonen, A.: The Arctic has warmed nearly four times faster

than the globe since 1979, Commun. Earth Environ., 3, https://doi.org/10.1038/s43247-022-00498-3, 2022.

Schneider von Deimling, T., Meinshausen, M., Levermann, A., Huber, V., Frieler, K., Lawrence, D. M., and Brovkin, V.: Estimating the near-surface permafrost-carbon feedback on global warming, Biogeosciences, 9, 649–665, https://doi.org/10.5194/bg-9-649-2012, 2012.

Schulzweida, U.: CDO User Guide, Zenodo, https://doi.org/10.5281/zenodo.10020800, 2023.

Schuur, E. A. G., Abbott, B. W., Commane, R., Ernakovich, J., Euskirchen, E., Hugelius, G., Grosse, G., Jones, M., Koven, C., Leshyk, V., Lawrence, D., Loranty, M. M., Mauritz, M., Olefeldt, D., Natali, S., Rodenhizer, H., Salmon, V., Schädel, C., Strauss, J., Treat, C., and Turetsky, M.: Permafrost and Climate Change: Carbon Cycle Feedbacks From the Warming Arctic, Annu. Rev. Environ. Resour., 47, 343–371, https://doi.org/10.1146/annurev-environ-012220-011847, 2022.

Séférian, R., Nabat, P., Michou, M., Saint-Martin, D., Voldoire, A., Colin, J., Decharme, B., Delire, C., Berthet, S., Chevallier, M., Sénési, S., Franchisteguy, L., Vial, J., Mallet, M., Joetzjer, E., Geoffroy, O., Guérémy, J.-F., Moine, M.-P., Msadek, R., Ribes, A., Rocher, M., Roehrig, R., Salas-y Mélia, D., Sanchez, E., Terray, L., Valcke, S., Waldman, R., Aumont, O., Bopp, L., Deshayes, J., Éthé, C., and Madec, G.: Evaluation of CNRM Earth System Model, CNRM-ESM2-1: Role of Earth System Processes in Present-Day and Future Climate, J. Adv. Model. Earth Sy., 11, 4182–4227, https://doi.org/10.1029/2019MS001791, 2019.

Sellar, A. A., Jones, C. G., Mulcahy, J. P., Tang, Y., Yool, A., Wiltshire, A., O'Connor, F. M., Stringer, M., Hill, R., Palmieri, J., Woodward, S., de Mora, L., Kuhlbrodt, T., Rumbold, S. T., Kelley, D. I., Ellis, R., Johnson, C. E., Walton, J., Abraham, N. L., Andrews, M. B., Andrews, T., Archibald, A. T., Berthou, S., Burke, E., Blockley, E., Carslaw, K., Dalvi, M., Edwards, J., Folberth, G. A., Gedney, N., Griffiths, P. T., Harper, A. B., Hendry, M. A., Hewitt, A. J., Johnson, B., Jones, A., Jones, C. D., Keeble, J., Liddicoat, S., Morgenstern, O., Parker, R. J., Predoi, V., Robertson, E., Siahaan, A., Smith, R. S., Swaminathan, R., Woodhouse, M. T., Zeng, G., and Zerroukat, M.: UKESM1: Description and Evaluation of the U.K. Earth System Model, J. Adv. Model. Earth Sy., 11, 4513–4558, https://doi.org/10.1029/2019MS001739, 2019.

Shindell, D. T., Schmidt, G. A., Mann, M. E., and Faluvegi, G.: Dynamic winter climate response to large tropical volcanic eruptions since 1600, J. Geophys. Res.-Atmos., 109, https://doi.org/10.1029/2003jd004151, 2004.

Shupe, M. D. and Intrieri, J. M.: Cloud Radiative Forcing of the Arctic Surface: The Influence of Cloud Properties, Surface Albedo, and Solar Zenith Angle, J. Climate, 17, 616–628, 2004.

Stieglitz, M., Déry, S. J., Romanovsky, V. E., and Osterkamp, T. E.: The role of snow cover in the warming of arctic permafrost, Geophys. Res. Lett., 30, https://doi.org/10.1029/2003GL017337, 2003.

Strauss, J., Schirrmeister, L., Grosse, G., Fortier, D., Hugelius, G., Knoblauch, C., Romanovsky, V., Schädel, C., Schneider von Deimling, T., Schuur, E. A. G., Shmelev, D., Ulrich, M., and Veremeeva, A.: Deep Yedoma permafrost: A synthesis of depositional characteristics and carbon vulnerability, Earth-Sci. Rev., 172, 251–271, https://doi.org/10.1016/j.earscirev.2017.07.007, 2017.

Sturm, M.: Changing snow and shrub conditions affect albedo with global implications, J. Geophys. Res., 110, https://doi.org/10.1029/2005jg000013, 2005.

Tilmes, S., Mills, M. J., Niemeier, U., Schmidt, H., Robock, A., Kravitz, B., Lamarque, J.-F., Pitari, G., and English, J. M.: A new Geoengineering Model Intercomparison Project (GeoMIP) experiment designed for climate and chemistry models, Geosci. Model Dev., 8, 43–49, https://doi.org/10.5194/gmd-8-43-2015, 2015.

Van Huissteden, J.: Thawing permafrost: Permafrost carbon in a warming arctic, Springer International Publishing, 1–508 pp., https://doi.org/10.1007/978-3-030-31379-1, 2020.

Visioni, D., MacMartin, D. G., Kravitz, B., Tilmes, S., Mills, M. J., Richter, J. H., and Boudreau, M. P.: Seasonal Injection Strategies for Stratospheric Aerosol Geoengineering, Geophys. Res. Lett., 46, 7790–7799, https://doi.org/10.1029/2019GL083680, 2019.

Visioni, D., MacMartin, D. G., Kravitz, B., Boucher, O., Jones, A., Lurton, T., Martine, M., Mills, M. J., Nabat, P., Niemeier, U., Séférian, R., and Tilmes, S.: Identifying the sources of uncertainty in climate model simulations of solar radiation modification with the G6sulfur and G6solar Geoengineering Model Intercomparison Project (GeoMIP) simulations, Atmos. Chem. Phys., 21, 10039–10063, https://doi.org/10.5194/acp-21-10039-2021, 2021.

Visioni, D., Kravitz, B., Robock, A., Tilmes, S., Haywood, J., Boucher, O., Lawrence, M., Irvine, P., Niemeier, U., Xia, L., Chiodo, G., Lennard, C., Watanabe, S., Moore, J. C., and Muri, H.: Opinion: The scientific and community-building roles of the Geoengineering Model Intercomparison Project (GeoMIP) – past, present, and future, Atmos. Chem. Phys., 23, 5149–5176, https://doi.org/10.5194/acp-23-5149-2023, 2023.

Zhao, M., Cao, L., Visioni, D., and MacMartin, D. G.: Carbon Cycle Response to Stratospheric Aerosol Injection With Multiple Temperature Stabilization Targets and Strategies, Earth's Future, 12, https://doi.org/10.1029/2024EF004474, 2024.

Zwiers, F. W. and von Storch, H.: Taking Serial Correlation into Account in Tests of the Mean, J. Climate, 8, 336–351, https://doi.org/10.1175/1520-0442(1995)008<0336:TSCIAI>2.0.CO;2, 1995.

The Geoengineering Model Intercomparison Project (GeoMIP): The Geoengineering Model Intercomparison Project (GeoMIP) – About, http://climate.envsci.rutgers.edu/geomip/about.html, last access: 24 May 2023.